Identification of essential sites of lipid peroxidation in ferroptosis

Check for updates

A. Nikolai von Krusenstiern[1], Ryan N. Robson [2], Naixin Qian[3], Baiyu Qiu[1], Fanghao Hu [3], Eduard Reznik[1], Nailah Smith [1], Fereshteh Zandkarimi[3], Verna M. Estes[2], Marcel Dupont[1], Tal Hirschhorn[1], Mikhail S. Shchepinov[4], Wei Min [3] ✉, K. A. Woerpel [2] ✉ & Brent R. Stockwell [1,3] ✉

Ferroptosis, an iron-dependent form of cell death driven by lipid peroxidation, provides a potential treatment avenue for drug-resistant cancers and may play a role in the pathology of some degenerative diseases. Identifying the subcellular membranes essential for ferroptosis and the sequence of their peroxidation will illuminate drug discovery strategies and ferroptosis-relevant disease mechanisms. In this study, we employed fluorescence and stimulated Raman scattering imaging to examine the structure–activity–distribution relationship of ferroptosis-modulating compounds. We found that, although lipid peroxidation in various subcellular membranes can induce ferroptosis, the endoplasmic reticulum (ER) membrane is a key site of lipid peroxidation. Our results suggest an ordered progression model of membrane peroxidation during ferroptosis that accumulates initially in the ER membrane and later in the plasma membrane. Thus, the design of ER-targeted inhibitors and inducers of ferroptosis may be used to optimally control the dynamics of lipid peroxidation in cells undergoing ferroptosis.

The iron-dependent form of lipid-peroxidation-mediated cell death known as ferroptosis, although remaining somewhat enigmatic, represents an emerging modality for treatment of several illnesses, including cancers and degenerative diseases[1–5]. There is a suite of compounds that induce and inhibit this form of regulated cell death, highlighting the therapeutic potential of controlling this mechanism of cell death. Induction of ferroptosis, pharmacologically or genetically, has been shown to slow and regress tumor growth in vivo[6,7]. In addition, some approved medications may kill cancer cells by ferroptosis, albeit not with high selectivity[8–11]. Compounds inhibiting ferroptosis have shown therapeutic potential in models of degenerative diseases and ischemia-reperfusion injuries[12–18]. The development of potent and selective ferroptosis-inducing or ferroptosis-inhibiting drugs will benefit from a deeper understanding of the mechanisms of this form of cell death.

Ferroptosis occurs when lipid hydroperoxides accumulate in cellular membranes[19–21]. The increased accumulation of such hydroperoxides can be due to inhibition of lipid reactive oxygen species (ROS) detoxification systems or by direct lipid ROS generation[12,22–24]. Polyunsaturated fatty acyl (PUFA) moieties, incorporated into phospholipids, are specific substrates of iron-dependent peroxidation during ferroptosis due to their easily abstractable bis-allylic hydrogens[21,25,26]. Because PUFA moieties could be incorporated into membranes throughout the cell, the question of which cellular membranes are particularly susceptible to, or necessary for, ferroptosis is still enigmatic. Previous work exploring the distribution of ferrostatin-1 (fer-1), an anti-ferroptotic agent, revealed that, although fer-1 localizes to the endoplasmic reticulum (ER) membrane, mitochondrial membranes and lysosomal membranes, accumulation in neither the mitochondria nor the lysosomes was necessary for activity, suggesting that the ER membrane

[1]Department of Biological Sciences, Columbia University, New York, NY, USA. [2]Department of Chemistry, New York University, New York, NY, USA. [3]Department of Chemistry, Columbia University, New York, NY, USA. [4]Retrotope, Inc., Los Altos, CA, USA. ✉e-mail: wm2256@columbia.edu; kwoerpel@nyu.edu; bstockwell@columbia.edu

may serve as a primary site of action for this compound[27]. The role of mitochondria in ferroptosis was further explored by Gao et al.[28], who found that mitochondria play a role in cysteine-deprivation-induced ferroptosis, but they are dispensable for GPX4-inhibition-induced ferroptosis. Additionally, work by Mao et al.[29] identified that inhibition of the mitochondrial reductase dihydroorotate dehydrogenase (DHODH) sensitizes cells to ferroptosis, indicating another role for mitochondria in the proliferation of lipid peroxides in ferroptotic death.

The plasma membrane (PM) has also been implicated in ferroptosis. The anti-ferroptotic effect of the monounsaturated fatty acid (MUFA) oleic acid was observed to be exerted in conjunction with accumulation in the PM[30]. Furthermore, the protein FSP1/AIFM2 was discovered to act as a CoQ_{10}-dependent suppressor of ferroptosis, possibly working at the PM[31,32]. These prior studies raised the question of which cellular membranes are involved in the ferroptotic death process and how they are interrelated. In the present study, we aimed to elucidate the roles of cellular membranes in ferroptotic death.

To identify essential membranes for ferroptosis, we evaluated the structure–activity–distribution profile of ferroptosis inhibitors and inducers. This new approach involves imaging the subcellular distribution of ferroptosis-modulating compounds and then generating analogs with altered distributions or genetically and pharmacologically modulating the compounds' sites of accumulation. Two imaging techniques were used in this work: confocal fluorescence microscopy of compounds with fluorescent tags and stimulated Raman scattering (SRS) imaging of Raman-active compounds with high sensitivity and resolution[33,34]. Although fluorescence imaging is more commonly employed and highly sensitive, SRS imaging offers the advantage of requiring only minor or even no modifications to the structures of the molecules of interest. Compared to conventional confocal Raman microscopy, SRS offers orders of magnitude higher imaging speed and sensitivity. Furthermore, SRS represents an orthogonal technique to fluorescence imaging, thereby eliminating interference during fluorescence measurement of cellular stains.

The primary ferroptosis-modulating compounds explored in this study were ferroptosis-inhibiting polyunsaturated fatty acids deuterated at their bis-allylic sites (D-PUFAs) and ferroptosis-inducing class IV inducers, including $FINO_2$ and related compounds.

D-PUFAs potently inhibit ferroptosis due to the primary kinetic isotope effect. Bis-allylic hydrogens, situated between two double bonds, are particularly prone to hydrogen atom abstraction, which results in carbon oxygenation and subsequent lipid peroxide formation. In contrast, heavier deuterium atoms at the same sites slow this abstraction sufficiently to block peroxide propagation[35,36]. The potent anti-peroxidation activity of these compounds has been demonstrated in vitro as well as in vivo[17,24,35–38]. Here, we aimed to use these D-PUFAs as a chemical tool, hypothesizing that the observed sites of accumulation may point to essential protection points against ferroptosis.

We also explored the class IV ferroptosis inducer $FINO_2$, which is an endoperoxide-containing 1,2-dioxolane that induces ferroptosis through oxidation of iron and indirect inactivation of GPX4 (ref. [24]). Because $FINO_2$ is a lipophilic compound, we hypothesized that $FINO_2$ accumulates in membranes and directly induces PUFA peroxidation in PUFA-containing phospholipids (PUFA-PLs) in those locations. Other ferroptosis inducers target specific proteins and disrupt anti-ferroptotic pathways, meaning that their localization is not directly connected to sites of lipid peroxide formation. However, because $FINO_2$ directly delivers a peroxide to cells, its subcellular localization is of interest. We, therefore, aimed to determine if $FINO_2$ targets specific membranes that allow it to exert its pro-ferroptotic action and whether redirection to other subcellular sites would alter the ability of $FINO_2$-type compounds to induce ferroptosis.

We report here the analysis of subcellular distributions of numerous fatty acids and class IV ferroptosis inducers, finding that lipid peroxidation in the ER membrane and PM is essential to ferroptosis,

with a contribution from the mitochondria. We determined that modulating the lipid composition of these membranes alters cell sensitivity to ferroptosis. We found that ferroptosis can be induced through lipid peroxidation in various organelles. Finally, we observed a consistent pattern of lipid ROS spread in cells treated with all four classes of ferroptosis inducers: lipid peroxidation initially propagated through the ER membrane and later accumulated in the PM. Together, these results identify the ER membrane as a key site of ferroptotic lipid peroxidation and an important target of ferroptosis-inducing and ferroptosis-inhibiting compounds.

Results

Deuterated PUFAs accumulate perinuclearly and in puncta
D-PUFAs will potently inhibit ferroptosis due to the primary kinetic isotope effect—heavier deuterium atoms at these sites slow the abstraction sufficiently to block peroxide propagation[35,36]. We reasoned that identifying the subcellular sites of accumulation of D-PUFAs would reveal essential sites of lipid peroxidation in ferroptotic death.

We evaluated the potency and distribution of three different D-PUFAs: arachidonic acid-d_6 (ARA-d_6), eicosapentaenoic acid-d_8 (EPA-d_8) and docosahexaenoic acid-d_{10} (DHA-d_{10}) (Fig. 1a). Treatment with 20 µM of ARA-d_6, EPA-d_8 or DHA-d_{10} potently prevents death by all four classes of ferroptosis inhibitors (Fig. 1b), and concentrations as low as 1 µM were sufficient to cause some suppression of cell death (Extended Data Fig. 1a).

To determine the subcellular sites of accumulation of D-PUFAs, we made use of SRS imaging[33,34]. Because the vibration of C–D bonds is Raman active in a cell-silent region, it is possible to directly image these C–D-containing D-PUFAs with high specificity, sensitivity and spatial resolution inside living cells. Imaging of DHA-d_{10} in HT-1080 fibrosarcoma cells revealed perinuclear accumulation (Fig. 1c, white arrow) decorated with bright puncta (Fig. 1c, red arrow). This distribution was also observed for ARA-d_6 and EPA-d_8 (Fig. 1d) as well as in other cell types (Fig. 1e), including Panc-1 (a human pancreatic cancer line), N27 (a rat dopaminergic neuronal line) and HT-22 (a mouse hippocampal neuronal line) cells. Thus, D-PUFAs have a consistent and predominant perinuclear and punctal localization. This concentration of each of these PUFAs was sufficient to inhibit ferroptosis by all four classes of inducers, indicating that the areas of accumulation were candidates for primary activity sites.

D-PUFAs in lipid droplets do not inhibit ferroptosis
We hypothesized that the puncta observed by SRS imaging of D-PUFAs were either lipid droplets or lysosomes. Cells treated with DHA-d_{10} were stained with LysoTracker to label lysosomes and Nile Red to label lipid droplets. These experiments revealed that DHA-d_{10} accumulates in lipid droplets but not in lysosomes (Fig. 2a). We did not observe D-PUFA accumulation in peroxisomes (Extended Data Fig. 1b). Lipidomic analysis of cells treated with DHA-d_{10} supported localization in lipid droplets, as the PUFA was incorporated into triacylglycerides (TAGs) and cholesterol esters (CEs), which are stored in lipid droplets (Fig. 2b).

We next aimed to determine whether the accumulation in lipid droplets was relevant to the anti-ferroptotic activity of D-PUFAs. To inhibit lipid droplet formation, synthesis of TAGs was blocked by pharmacologically inhibiting diglyceride acyltransferase (DGAT) enzymes. A co-treatment with 1 µM of inhibitors of each DGAT isozyme (PF-06424439 and A922500) completely abated lipid droplet accumulation in cells treated with exogenous PUFAs, as demonstrated by SRS imaging (Fig. 2c). Inhibition of lipid droplet formation by DGAT inhibitors had no impact on the anti-ferroptotic potency of DHA-d_{10} (Fig. 2d), demonstrating that accumulation in lipid droplets does not play a role in the ability of D-PUFAs to prevent ferroptosis and, moreover, that lipid droplets are not needed for ferroptosis.
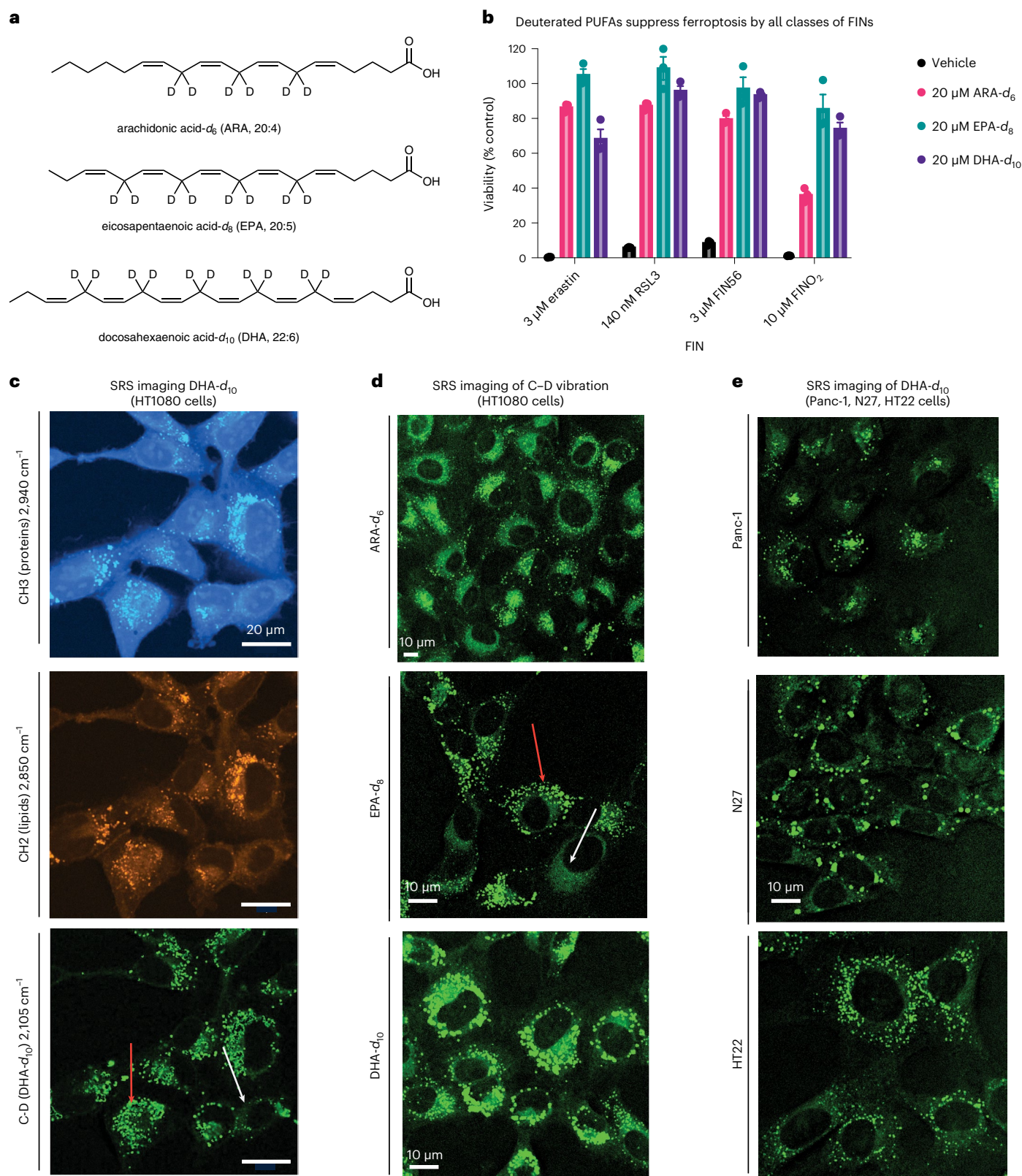
Fig. 1 | Exogenous D-PUFAs rescue ferroptosis and accumulate perinuclearly and in puncta. a, Structures of D-PUFAs. **b**, Rescue of HT-1080 cells treated with each of four classes of ferroptosis inducers after a 24-hour pre-treatment with D-PUFAs. Data are represented as mean ± s.e.m., $n = 3$. **c**, SRS images of HT-1080 cells treated for 24 hours with 20 μM DHA-d_{10}. The protein (CH3) and lipid (CH2) cell-intrinsic vibrational frequencies are shown as well for comparison. Red arrow points to lipid droplets; white arrow points to perinuclear accumulation. **d**, SRS imaging of HT-1080 cells treated for 24 hours with the three different D-PUFAs used in this study: ARA-d_6 (80 μM), EPA-d_8 (20 μM) and DHA-d_{10} (20 μM). Red arrow points to lipid droplets; white arrow points to perinuclear accumulation. **e**, SRS imaging of Panc-1, N27 and HT-22 cells treated for 24 hours with 20 μM DHA-d_{10}.
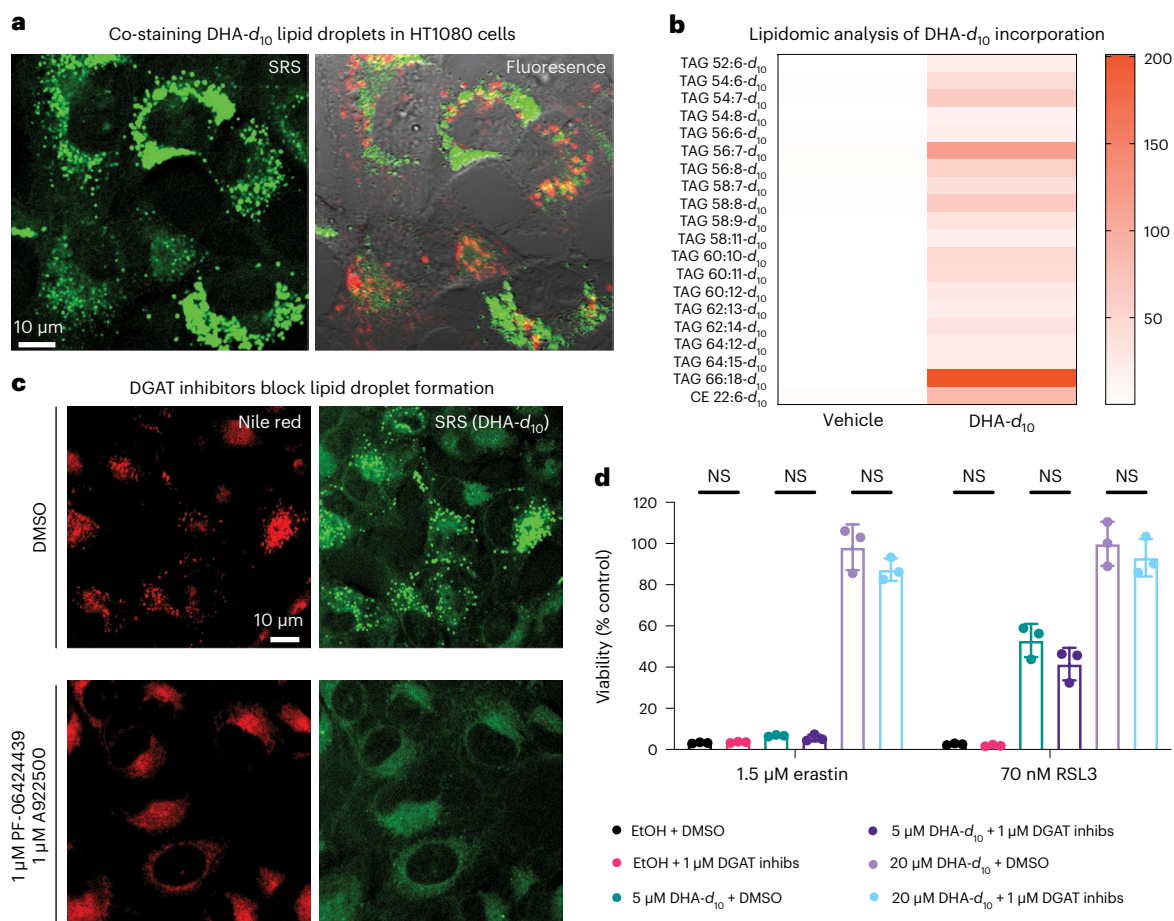
Fig. 2 | D-PUFA accumulation in lipid droplets does not play a role in inhibition of ferroptosis. a, SRS and fluorescence imaging of HT-1080 cells treated with 20 µM DHA-d_{10} and then stained with Nile Red (shown in green for consistency with SRS image) and LysoTracker Green (in red). **b**, Heat map showing relative incorporation of deuterated DHA into HT-1080 triglycerides, as measured by LC–MS. Vehicle showed no deuterated incorporation, whereas DHA-d_{10} had varying levels of incorporation into TAGs and CEs, with different sum total numbers of carbons and double bonds. Data shown are an average of absolute signal intensity of three biological replicates. **c**, SRS and fluorescence imaging of HT-1080 cells treated with DHA-d_{10} (20 µM) ± co-treatment with DGAT inhibitors PF-06424439 (1 µM) and A922500 (1 µM) and then stained with Nile Red. **d**, Rescue of HT-1080 cells from erastin or RSL3 lethality with pre-treatment of DHA-d_{10} ± co-treatment of DGAT inhibitors. Data are represented as mean ± s.e.m., along with individual data points, $n = 3$. Statistics were performed using two-sided unpaired t-test. LC–MS, liquid chromatography–mass spectrometry.

D-PUFAs incorporate primarily into ER phospholipids

We next aimed to determine the identity of the perinuclear site of accumulation of D-PUFAs. Upon inhibition of lipid droplet formation, it became clear that D-PUFAs were likely accumulating in the ER membrane. This hypothesis was confirmed by SRS imaging of cells treated with DHA-d_{10} (with and without co-treatment of DGAT inhibitors) and stained with ER-Tracker Green, a fluorescent ER label (Fig. 3a). To determine whether D-PUFAs were additionally accumulating in the Golgi body membrane, cells treated with DHA-d_{10} were co-stained with ER-Tracker and BODIPY TR Ceramide, a fluorescent Golgi stain. The resulting correlative fluorescence and SRS images enhanced by x–z and y–z axis images revealed that accumulation of D-PUFAs occurs primarily in the ER membrane, with little co-localization of DHA-d_{10} with the Golgi stain (Fig. 3b, white arrows). Finally, lipidomic analysis showed incorporation of DHA-d_{10} into phospholipids (Fig. 3c). There was marked incorporation into phosphatidylethanolamine (PE) phospholipids and ether phospholipids. Ferroptosis has been reported to involve PE phospholipids[20]; thus, incorporation of D-PUFAs into PEs with an observed ER distribution potentially explains the potent protective effect of these fatty acids. With regard to ether phospholipids, plasmalogens have been implicated in ferroptosis,

with observations that ether phospholipids containing PUFAs are substrates of lipid peroxidation during ferroptosis[39] and that plasmalogen synthesis proteins are necessary for some fatty-acid-induced ferroptosis[40].

Given the nuanced role of mitochondria in ferroptosis and the proximity of the ER and mitochondria, we sought to determine incorporation of D-PUFAs into mitochondria. Initial images did not show overlap with mitochondria, and higher-resolution SRS imaging showed a distribution pattern more consistent with ER localization than mitochondrial localization (Extended Data Fig. 1c,d). Due to the proximity of the ER and mitochondria in these images, however, it was difficult to accurately quantify ER versus mitochondrial incorporation definitively. We, therefore, attempted an orthogonal approach, by treating cells with D-PUFA and purifying ER and mitochondrial membranes. We quantified relative incorporation of D-PUFA using high-resolution mass spectrometry (Extended Data Fig. 1d,e) and found that there was a significantly greater normalized incorporation into the ER as compared to the mitochondria. Notably, we observed contamination of the mitochondrial fraction with ER as measured by the ER-resident protein PDI on western blot, suggesting that the true D-PUFA level in the mitochondria is even lower. We conclude that the perinuclear
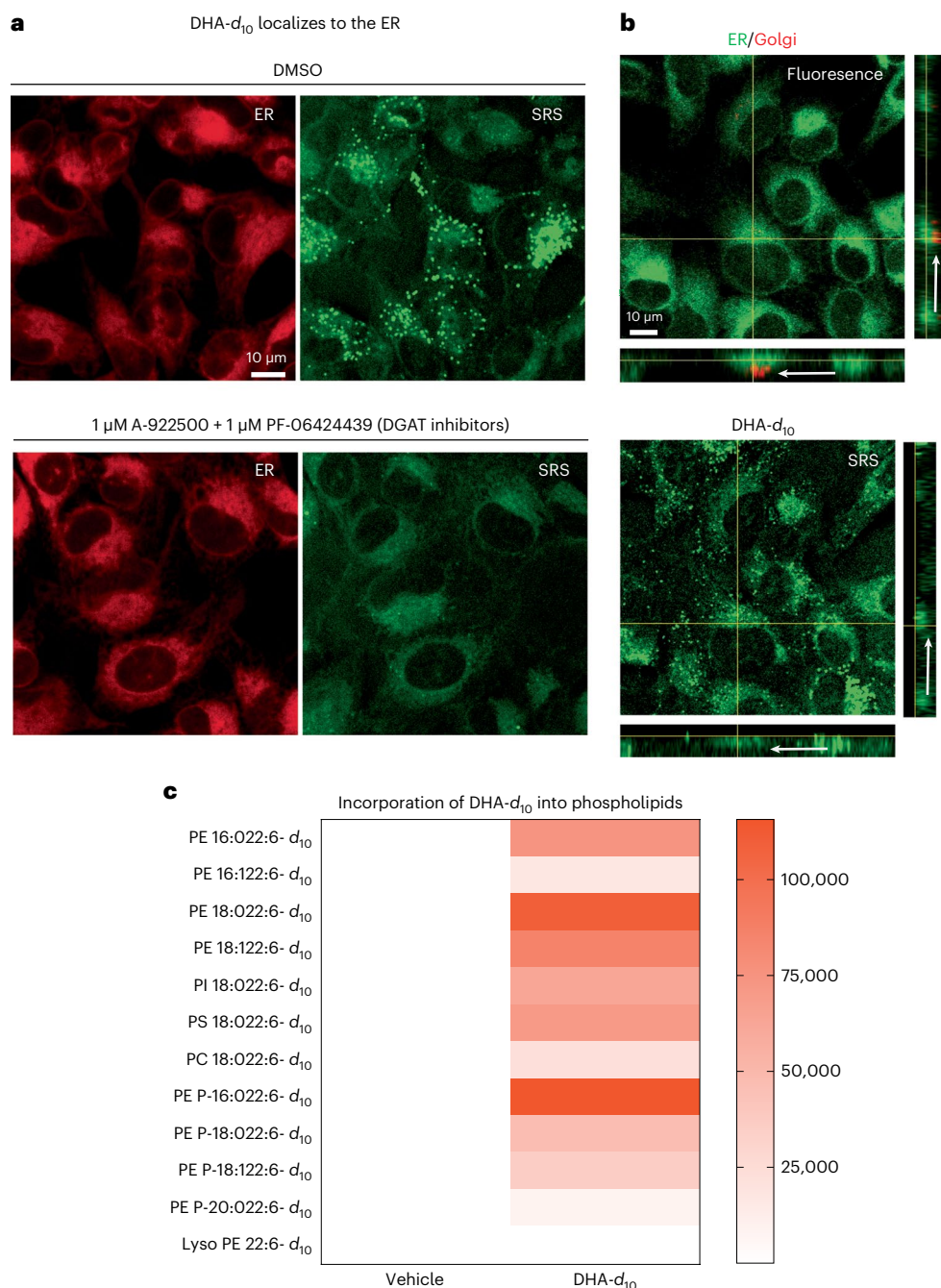
Fig. 3 | Anti-ferroptotic D-PUFAs incorporate into ER PE phospholipids and ether phospholipids. a, SRS and fluorescence imaging of HT-1080 cells treated with DHA-d_{10} (20 μM) ± co-treatment with DGAT inhibitors PF-06424439 (1 μM) and A922500 (1 μM) and then stained with ER-Tracker Green. **b**, SRS and fluorescence imaging of HT-1080 cells treated with DHA-d_{10} (20 μM) and then stained with ER-Tracker Green and BODIPY TR Ceramide (a Golgi stain). White arrows indicate the Golgi region. **c**, Heat map showing incorporation of deuterated DHA into HT-1080 phospholipids as measured by LC–MS. Vehicle shows no deuterated incorporation, whereas DHA-d_{10} has varying incorporation depending on the lipid species and fatty acid compositions. PC, phosphatidylcholine; PI, phosphatidylinositol; PS, phospatidyserine. Data shown are an average of absolute signal intensity of three biological replicates. LC–MS, liquid chromatography–mass spectrometry.

localization of D-PUFAs is primarily in the ER, but we cannot rule out minor incorporation into the mitochondria.

We made extensive attempts to modulate the ER through genetic and pharmacological means. None of the approaches explored, however, resulted in significant or persistent changes in ER size or composition. Knockdown of lipid metabolism genes, including acyl-CoA synthase (*ACSL*) genes and 1-acylglycerol-3-phosphate O-acyltransferase 3 (*AGPAT3*), did cause decreases in D-PUFA potency

(Extended Data Fig. 2a–c), but these effects were not consistent. A decrease in PUFA incorporation was not reliably detected under these conditions (Extended Data Fig. 2d). We attempted to alter incorporation of exogenous lipids into the ER with various compounds, including thimerosal, a lysophosphatidylcholine acyltransferase (LPCAT) inhibitor[41]; miltefosine, a phosphatidylcholine synthesis inhibitor[42]; and *N*-ethylmaleimide, a phospholipase A2 (PLA2) activator[43]. None of these modulators was effective, however (Extended Data Fig. 3a–c).

We also tried to increase the ER size by inhibiting ER-phagy pathways and to decrease ER area by directing organelle-depleting proteins to the ER. Knockdown of ER-phagy proteins FAM134B, SEC62 and RTN3 (ref. [44]) did result in an increase sensitivity to FINs, but there was no detectable expansion of ER volume (Extended Data Fig. 3d–f). Considering that PLA2G16 and FUN14 domain-containing 1 (FUNDC1) both play roles in targeted organelle degradation[45,46], we overexpressed these proteins on the surface of the ER to induce ER-phagy. GFP, PLA2G16, FUNDC1 and the active cytosolic N-terminal region of FUNDC1 were directed to the ER using a cytochrome B5 tag (Extended Data Fig. 4a–c), resulting in no detectable change in ER size. We concluded that modulation of ER size and lipid composition is challenging, and perhaps future developments will allow more straightforward and applicable manipulation of ER surface area and content.

Modulating ER and PM lipids alters ferroptotic sensitivity

We next sought to explore if the distribution observed for D-PUFAs remained consistent for other fatty acids relevant to ferroptosis. The fatty acids examined included pro-ferroptotic PUFAs and anti-ferroptotic MUFAs. We hypothesized that, if we enriched the ER membrane with these fatty acids, we would observe corresponding changes in sensitivity to ferroptosis.

To determine the distribution of PUFAs and MUFAs, SRS imaging was again employed. Fatty acids labeled with deuterium atoms were again used—PUFAs ARA-d_{11} and DHA-d_5, deuterated at non-bis-allylic sites (and, therefore, pro-ferroptotic with abstractable bisallylic hydrogens), and MUFAs oleic-d_{17} acid (OA-d_{17}) and palmitoleic-d_{13} acid (PA-d_{13}) (which are anti-ferroptotic due to their lack of bisallylic sites as they harbor a monounsaturated fatty acyl moiety) (Fig. 4a). All four fatty acids displayed the same distribution pattern as the anti-ferroptotic D-PUFAs (Fig. 4b). As a control, the distributions of two other lipids were tested as well: myristic-d_{27} acid (MA-d_{27}) and cholesterol-d_6. MA-d_{27}, a saturated fatty acid (SFA), accumulated into the ER and lipid droplets like other fatty acids, demonstrating that this distribution appears to be common to various fatty acid types, including SFAs that do not influence ferroptosis. Cholesterol-d_6 did not accumulate in the ER, demonstrating that the ER is not simply the default site of accumulation for any lipid (Extended Data Fig. 5a–c). Solution Raman spectra of all these compounds showed an observable C–D peak (Extended Data Fig. 5d).

Once the subcellular distributions of these lipids were assessed, their effects on ferroptotic death were evaluated. As expected, pre-treatment with the MUFAs OA-d_{17} or PA-d_{13} potently inhibited RSL3-induced ferroptosis, whereas PUFAs ARA-d_{11} and DHA-d_5 significantly increased cell death (Fig. 4c). By contrast, myristic acid and cholesterol did not significantly alter sensitivity to ferroptosis (Extended Data Fig. 5e). To increase incorporation of PUFAs into membranes via increased intracellular PUFA-CoA concentration, an HT-1080 ACSL4 overexpression cell line was generated (Extended Data Fig. 5f). HT-1080 ACSL4 OE cells exhibited increased sensitivity to ferroptosis, as well as an increased pro-ferroptotic effect of pre-treatment with PUFAs (Fig. 4d), confirming that enriching PUFAs in the ER enhanced ferroptosis. We also explored the possibility of localization of ACSL4 playing a role in PUFA distribution. Immunofluorescence imaging of HT-1080 cells stained for ACSL4, however, showed a distribution diffusely throughout cells (Extended Data Fig. 5g), with overlap with the ER, labeled by calnexin staining. A western blot of ER and mitochondrial fractions from HT-1080 cells identified ACSL4 in both fractions (Extended Data Fig. 5h), suggesting that ACSL4 is spread throughout the cell.

Because it has been observed that inhibition of OA incorporation into the PM correlated with diminished anti-ferroptotic effect of this MUFA[30], we sought to determine the degree of accumulation of MUFAs and PUFAs in the PM. Perhaps due to the narrowness of the PM in image cross-sections, as well as the lower magnification of the SRS images, no fatty acids were initially detected in the PM. Higher magnification, however, revealed PM incorporation. Staining with ER-Tracker Green

and FM 4-64 (PM) was used to generate ER and PM masks in MATLAB (Fig. 4e), which were then applied as masks to the SRS images of the deuterated FAs and used to quantify relative incorporation as compared to the general SRS lipid signal. We found that there was significantly more PUFA, MUFA and SFA incorporation into the ER than the PM, although relative levels were closer in the case of myristic acid (Fig. 4f).

Class IV ferroptosis inducers localize to ER and Golgi

To complement our work evaluating the key sites of ferroptosis-relevant fatty acid accumulation, we also explored the class IV ferroptosis inducer FINO$_2$ (**1**), which is an endoperoxide-containing 1,2-dioxolane that induces ferroptosis through oxidation of iron and indirect inactivation of GPX4 (ref. [24]). Because FINO$_2$ is a lipophilic compound, we hypothesized that FINO$_2$ accumulates in membranes and directly induces PUFA peroxidation in PUFA-PLs in those locations. We, therefore, aimed to determine if FINO$_2$ targets specific membranes that allow it to exert its pro-ferroptotic action and whether redirection to other subcellular sites would alter the ability of FINO$_2$-type compounds to induce ferroptosis.

To identify the subcellular distribution of FINO$_2$, labeled analogs were prepared. Peroxide FINO$_2$-1 (**2**) resembles FINO$_2$ but contains a fluorescent naphthalimide moiety (Fig. 5a) that can be visualized by fluorescence microscopy. Analog FINO$_2$-0 (**5**) does not contain the endoperoxide moiety essential for biological activity[24], but it does contain the naphthalimide moiety (Extended Data Fig. 6a). FINO$_2$-1 was able to induce ferroptosis with similar potency as FINO$_2$ (Fig. 5b), whereas FINO$_2$-0 did not induce ferroptosis (Extended Data Fig. 6b), confirming that the endoperoxide moiety is necessary and that the naphthalene group does not exhibit toxicity.

Next, confocal fluorescence imaging was performed to determine the distributions of these compounds. Because FINO$_2$-1 kills cells within a few hours of treatment, co-treatment with 3 μM of fer-1 was used to prevent cell death. As this co-treatment did not alter the distribution of the compound, co-treatment with fer-1 was used for the remainder of these analog imaging experiments (Extended Data Fig. 6c). FINO$_2$-1 displayed a perinuclear distribution that was confirmed to be the ER membrane (Fig. 5c). FINO$_2$-0 had the same distribution (Extended Data Fig. 6d). Accumulation in the Golgi membrane was identified as well (Fig. 5d).

To ensure that ER/Golgi membrane localization of FINO$_2$-1 was not due strictly to the addition of the fluorescent moiety, another analog, FINO$_2$-2 (**6**), was synthesized, which contained an SRS active diyne group instead of the naphthalimide fragment (Extended Data Fig. 6e). FINO$_2$-2 induced ferroptosis with similar potency as FINO$_2$-1 and FINO$_2$, and SRS imaging revealed that FINO$_2$-2 exhibited the same distribution as FINO$_2$-1 with some additional puncta (Extended Data Fig. 6f,g). Co-staining with LysoTracker and Nile Red was performed, showing that the puncta were neutral lipid bodies, likely induced by the higher concentrations necessary to detect the compound with SRS imaging (Extended Data Fig. 6g).

Finally, given the localization of fatty acids to the PM, we sought to determine if class IV ferroptosis inducers, such as FINO$_2$, accumulate to any extent in the PM. Cells treated with FINO$_2$-1 were co-stained with CellMask Deep Red to stain the PM and imaged (Extended Data Fig. 6h). FINO$_2$-1 did not show any overlap with CellMask, demonstrating that accumulation in the PM is not essential for initiation of ferroptosis by class IV inducers.

Ferroptosis can be directly induced in various organelles

Imaging of FINO$_2$-1 and FINO$_2$-0 revealed that delivery of an endoperoxide moiety to the ER and Golgi results in ferroptotic cell death. We wondered if redistributing an endoperoxide to other organelles would induce ferroptosis.

Experiments with a series of analogs of FINO$_2$ demonstrated that protection of the ER is key to inhibiting ferroptosis, regardless of where in the cell it was initiated. These analogs were synthesized
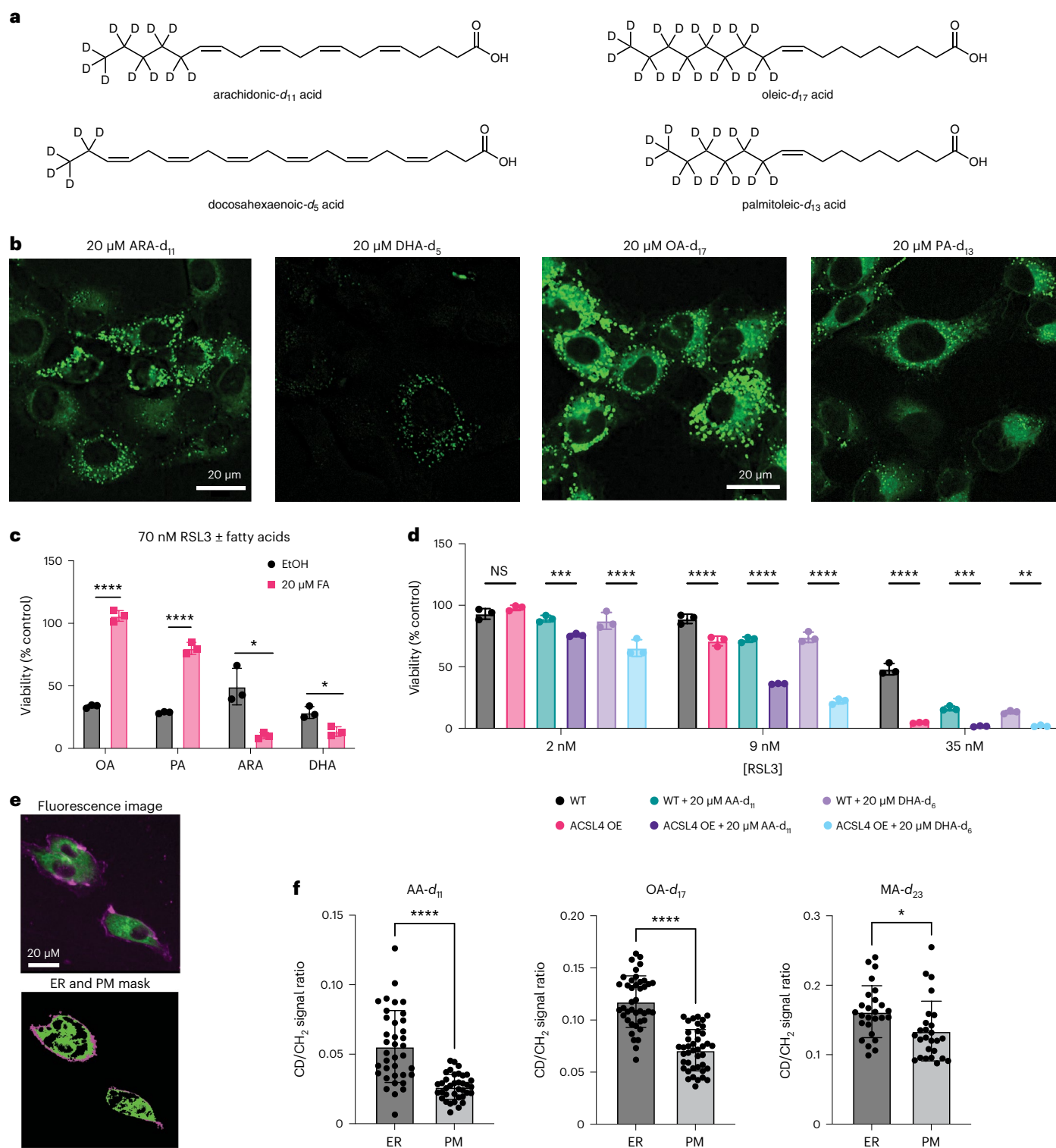
Fig. 4 | Enriching the ER and PM with pro-ferroptotic or anti-ferroptotic lipids modulates cell sensitivity to ferroptosis. a, Structures of deuterated fatty acids. Of note, the PUFAs are deuterated at non-bis-allylic positions and, therefore, do not inhibit ferroptosis. **b**, SRS images of HT-1080 cells treated with each of the deuterated fatty acids. **c**, Effect of pre-treatment (24 hours) with fatty acids on ferroptosis induced by RSL3 in HT-1080 cells, as compared to ethanol vehicle. Data are represented as mean ± s.e.m., $n = 3$. Two-sided unpaired t-test was performed with P values of 0.00001, 0.000053, 0.010389 and 0.012767. **d**, Increase in sensitivity to ferroptosis in cells overexpressing GFP-ACSL4 when treated with equivalent dose of PUFAs, as compared to parental HT-1080 cells. Data are represented as mean ± s.e.m., $n = 3$. Two-way ANOVA with Tukey's

multiple comparisons test was performed with P values of 0.5037, 0.0004, <0.0001, <0.0001, <0.0001, <0.0001, <0.0001, 0.0001 and 0.0033. **e**, Representative imaging of cells stained with ER-Tracker Green and FM 4-64 to label ER and PM, respectively, and the resulting masks generated in MATLAB. **f**, Quantification of relative fatty acid incorporation as C–D signal to general lipid CH$_2$ signal ratio within the PM and ER masks as shown in **e**. Data are represented as mean ± s.e.m., with each point representing an individual cell. Two-sided unpaired t-test resulted in ARA $n = 37$ $P < 0.0001$, OA $n = 41$ $P < 0.0001$ and MA $n = 26$ $P = 0.016$. For all panels, GraphPad Prism P value style of 0.1234 (NS), 0.0332 (*), 0.0021 (**), 0.0002 (***) and <0.0001 (****) was used. FA, fatty acid; NS, not significant; WT, wild-type.
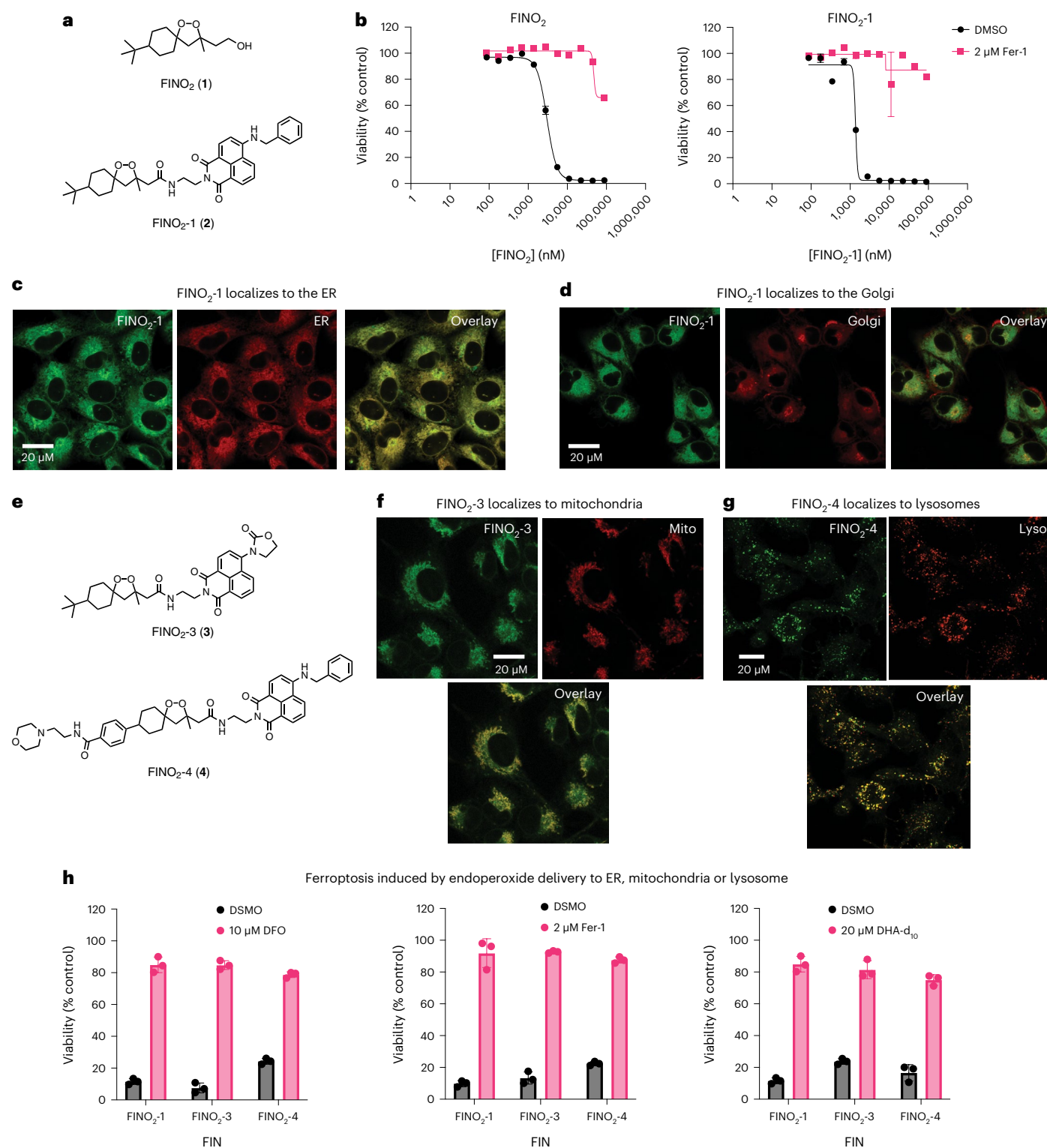
Fig. 5 | FINO$_2$ analogs can induce ferroptosis through accumulation in the ER, lysosome or mitochondria. a, Structures of FINO$_2$ and analog FINO$_2$-1 with an added fluorescent naphthalimide label. **b**, Dose–response curves of FINO$_2$ and FINO$_2$-1 ± fer-1 (2 µM). Data are represented as mean ± s.e.m., $n = 3$. **c**, Confocal fluorescence imaging of HT-1080 cells treated with FINO$_2$-1 (3 µM) and fer-1 (3 µM) for 3 hours, co-stained with ER-Tracker Red. **d**, Confocal fluorescence imaging of HT-1080 cells treated with FINO$_2$-1 (3 µM) and fer-1 (3 µM) for 3 hours, co-stained with BODIPY TR Ceramide. **e**, Structures of FINO$_2$ analogs FINO$_2$-3 and FINO$_2$-4.

f, Confocal fluorescence imaging of HT-1080 cells treated with FINO$_2$-3 (3 µM) and fer-1 (3 µM) for 3 hours, co-stained with MitoTracker Red CMXRos. **g**. Confocal fluorescence imaging of HT-1080 cells treated with FINO$_2$-4 (3 µM) and fer-1 (3 µM) for 3 hours, co-stained with LysoTracker Red. **h**, Rescue of HT-1080 cells treated for 24 hours with FINO$_2$-1 (2.5 µM), FINO$_2$-3 (5 µM) or FINO$_2$-4 (5 µM) by DFO (left, 10 µM co-treatment), fer-1 (center, 2 µM co-treatment) or DHA-d_{10} (right, 20 µM 24-hour pre-treatment). Data are represented as mean ± s.e.m., $n = 3$ biologically independent samples.

to redistribute the FINO$_2$ endoperoxide to other subcellular sites (Extended Data Fig. 7a). Although compounds FINO$_2$-5 (**7**) and FINO$_2$-6 (**8**) were successfully redirected to lysosomal membranes, they induced a non-ferroptotic cell death (Extended Data Fig. 7b,c). Compound FINO$_2$-7 (**9**) did not change distribution as compared to FINO$_2$-1 (Extended Data Fig. 7d). In contrast, FINO$_2$-3 (**3**) and FINO$_2$-4 (**4**) (Fig. 5e) successfully induced ferroptosis while being redistributed to the mitochondrial membranes and the lysosomal membranes, respectively (Fig. 5f,g). FINO$_2$-3 and FINO$_2$-4 did not accumulate in the PM when examined on higher magnification (Extended Data Fig. 6i) and retained similar lethal potency as FINO$_2$-1 (Extended Data Fig. 7e). Both FINO$_2$-3 and FINO$_2$-4 induced ferroptotic cell death that could be rescued by ferroptosis inhibitors with varying mechanisms and distributions: fer-1, deferoxamine and DHA-d_{10} (Fig. 5h). Rescue by both DHA-d_{10} and fer-1 points to the ER and mitochondria as essential sites of protection. As it has been demonstrated that mitochondria are not essential to ferroptosis[27,28], this finding implicates the ER as the key essential site of protection.

To further characterize the role of mitochondria, we sought to determine how treatment with these different FINO$_2$ analogs would impact sensitivity of cells to inhibition of the mitochondrial reductase DHODH. Inhibition of DHODH with the compound brequinar (BQR) induced ferroptosis in HT-1080 cells and caused an increase in sensitivity to RSL3, as previously demonstrated by Mao et al.[29] (Extended Data Fig. 8a). We then co-treated cells with a fixed amount of FINO$_2$-1, FINO$_2$-3 or FINO$_2$-4 and increasing doses of BQR (Extended Data Fig. 8b). FINO$_2$-1 demonstrated a greater degree of sensitization, suggesting that the combination of simultaneously oxidizing the ER and mitochondria more effectively induces ferroptosis.

Ferroptosis results in peroxidation of ER followed by PM

To further define the roles that different membranes play in the ferroptotic death cascade, HT-1080 cells were treated with inducers from each of the four ferroptosis classes and imaged at various timepoints to capture cell death progression. Cells were stained with C11 BODIPY to detect lipid peroxidation and organelle stains for subcellular localization.

In cells treated with ferroptosis inducers, we observed ER peroxidation initially, followed later by PM peroxidation (Fig. 6a,b). The peroxidation of each membrane was associated with morphological changes, including a decrease in ER membrane area and a narrowing and ballooning of the plasma membrane. ER peroxidation occurs within 2 hours for cells treated with RSL3, FIN56 and FINO$_2$. At this stage, there is not significant observable change in PM morphology (Fig. 6c). By 5 hours, most cells exhibited lipid peroxidation within the PM (Fig. 6d). Imidazole ketone erastin (IKE) induces a slower death than the other ferroptosis inducers; ER peroxidation was observed by 6 hours, with widespread PM peroxidation by 10 hours (Extended Data Fig. 8c,d).

To evaluate lipid peroxidation in the mitochondria, we compared correlation of oxidized C11 BODIPY signal to ER-Tracker versus MitoTracker. C11 BODIPY oxidized signal had a significantly higher correlation with the ER initially for all four FINs at the intial stages of death (Extended Data Fig. 8e). We performed the same quantification for cells treated with RSL3, BQR and RSL3 + BQR and observed more relative mitochondrial peroxidation with BQR as expected but, interestingly, still significantly greater peroxidation in the ER earlier in death (Extended Data Fig. 8f). Altogether, these data point to the ER as a primary essential target of lipid peroxidation in ferroptosis, with the peroxidation of the mitochondria and PM as a later stage of death.

Discussion

Previous research pointed to the ER membrane as a possible primary site of protection by fer-1 against lipid ROS to prevent ferroptotic death[27]. Here we demonstrated that directly introducing lipid ROS into the ER membrane is sufficient to initiate ferroptotic death, with our observation that the ER is the subcellular membrane target of FINO$_2$, a class IV ferroptosis inducer. It is not a requirement that lipid ROS be introduced exclusively to the ER membrane; however, we found that initiating lipid ROS in the mitochondrial or lysosomal membranes can still induce ferroptotic cell death, as demonstrated by the FINO$_2$ analogs FINO2-3 and FINO2-4, which localize to different subcellular compartments. Protecting lysosomes or mitochondria from lipid ROS with a radical trapping agent was not effective for blocking ferroptosis[27]. At the same time, inhibition of DHODH is known to fuel ferroptotic death, indicating a relevant contribution of mitochondrial ROS. Interestingly, we found that inhibiting DHODH in combination with induction of lipid ROS in the ER membrane with FINO$_2$-1 resulted in augmented cell death. Altogether, these findings indicate that ROS in the lysosomes and mitochondria can initiate and drive ferroptosis.

Our findings showed that lipid droplets do not play a significant role in D-PUFA-mediated protection against ferroptosis. Recently published work by Dierge et al.[47], however, found that exogenous n-3 and n-6 PUFAs potentiated ferroptosis in acidic cancer cells and that this effect is magnified through inhibition of protective shunting of PUFAs into lipid droplets with DGAT inhibitors. Therefore, although inhibition of lipid droplets may not influence sensitivity to ferroptosis in all cases, or play a role in the activity of anti-ferroptotic FAs, perturbation of lipid droplet metabolism may have a role in modulating ferroptosis in certain contexts.

Beyond lipid droplets, we identified the ER as the primary site of PUFA incorporation, with less incorporation into the PM or mitochondria. These results point to the ER, the largest membrane in the cell containing a high relative PUFA concentration, as a key target of lipid peroxidation in ferroptosis. We then aimed to deepen our understanding of the subcellular dynamics of lipid peroxidation to disentangle the roles of these membranes in influencing ferroptosis. For all ferroptosis inducers, PM lipid peroxidation was observed by C11-BODIPY 3–4 hours after ER lipid peroxidation was observed. This finding is consistent with previous observations by Magtanong et al.[30], who found that treatment with erastin2, an erastin analog, resulted in PM peroxidation 10 hours after treatment, as observed in our time-course for IKE. Our data indicate that ER peroxidation happens early in ferroptotic death, with mitochondrial and PM peroxidation as later events.

Our model proposes that the ER membrane is a key site of lipid peroxidation in ferroptosis induced by class I through class IV compounds. This finding couples with the previously observed activation of the ER stress-related unfolded protein response in ferroptosis and further underscores the role this organelle plays in ferroptosis[48,49]. Lipid peroxidation may spread from the ER to other membranes, or peroxidation of membranes may occur independently at different stages and with different rates. If lipid peroxidation is spreading, how it spreads is not clear. Vesicular transport or membrane contact sites are both good hypotheses and warrant further exploration. It was recently shown by Riegman et al.[50] that ferroptotic cell lysis is osmotic, and perhaps it is the combination of lipid peroxidation in the cell membrane and the osmotic swelling that results in the final blow of cell death—a membrane that is both stretched and then weakened finally pops.

In summary, we found that endoperoxide delivery to different organelle membranes can induce ferroptosis and that the ER membrane is a primary target of lipid peroxidation in ferroptotic death. Although mitochondria are not required for ferroptosis, when present they play an important role in susceptibility. We also observe that oxidation of the PM occurs at a later, more final stage of ferroptotic death. These observations dovetail with the cell's natural systems of protection against lipid peroxidation, with GPX4 serving as protector of the ER membrane and subcellular membranes in general, whereas DHODH protects the mitochondria, and FSP1 protects the PM[29,31,32]. The use of SRS and fluorescence imaging to examine the structure–activity–distribution relationship of inducers and inhibitors of ferroptosis demonstrates the power of such a strategy in its ability to demystify the
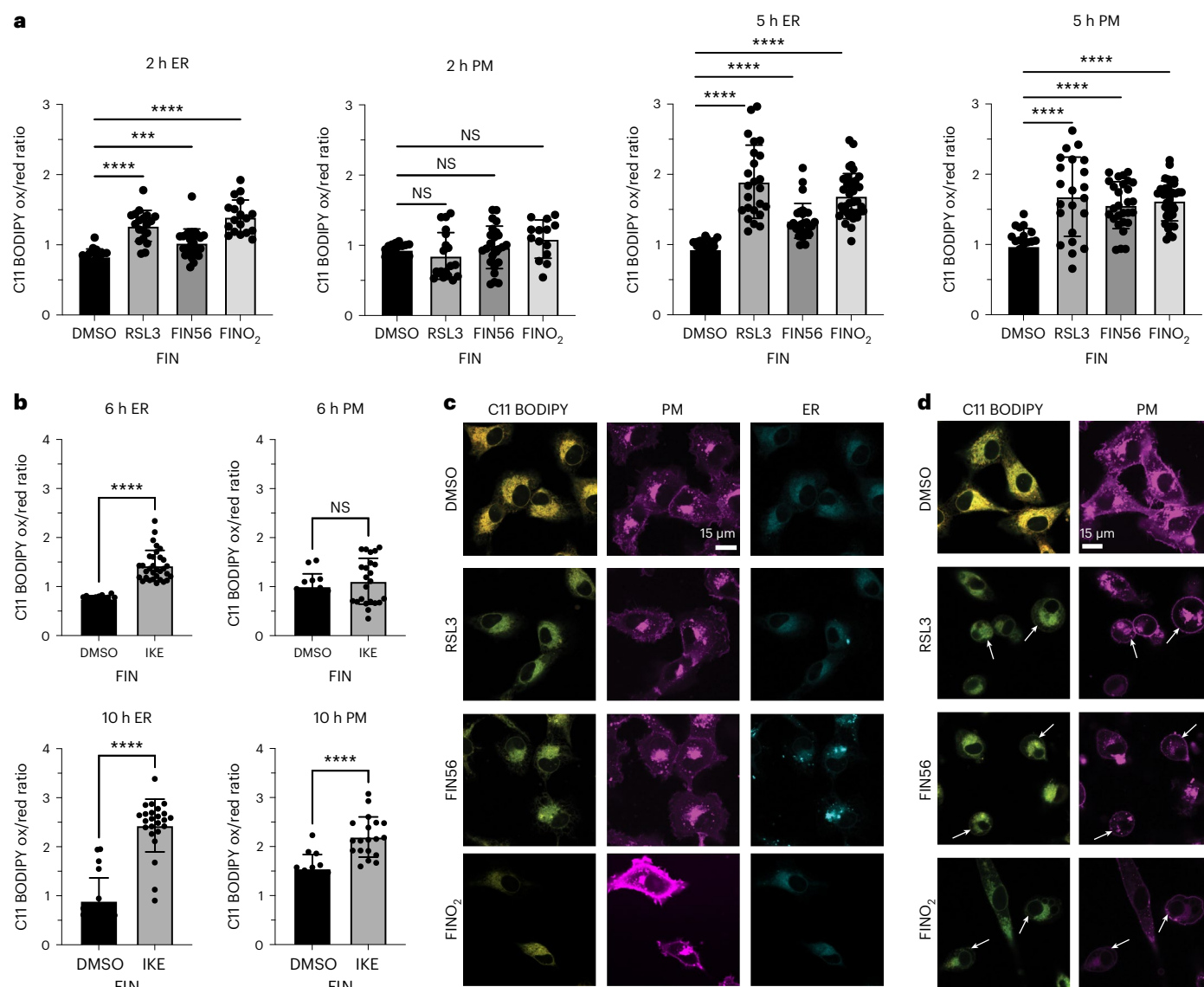
Fig. 6 | Ferroptosis induced by RSL3, FIN56, FINO$_2$ or IKE results in ER peroxidation followed by PM peroxidation. a, Quantification of C11 BODIPY oxidized:reduced ratio within the ER and PM of HT-1080 cells treated with DMSO, RSL3 (0.5 µM), FIN56 (10 µM) or FINO$_2$ (10 µM) at 2 hours and 5 hours. CellMask Deep Red (PM) and ER-Tracker Blue-White (ER) were used to select regions of interest in CellProfiler within which C11 BODIPY signal was quantified. Data are represented as mean ± s.e.m., with each point representing a single cell. Sample sizes are 2 hours ER (*n* = 18, 19, 25 and 18) and PM (*n* = 18, 19, 25 and 14) and 5 hours ER (*n* = 21, 24, 28 and 36) and PM (*n* = 21, 22, 28 and 36). Brown–Forsythe and Welch ANOVA with Dunnett T3 test for multiple comparisons was used with *P* values of: 2 hours ER (<0.0001, 0.0007 and <0.0001), 2 hours PM (0.6485, 0.9049 and 0.1531), 5 hours ER (<0.0001, <0.0001 and <0.0001) and 5 hours PM (<0.0001, <0.0001 and <0.0001). **b**, Quantification of C11 BODIPY oxidized:reduced ratio within the ER and PM of HT-1080 cells treated with DMSO or IKE (10 µM) at 6 hours and 10 hours. CellMask Deep Red (PM) and ER-Tracker

Blue-White (ER) were used to select regions of interest in CellProfiler within which C11 BODIPY signal was quantified. Data are represented as mean ± s.e.m., with each point representing a single cell. Sample sizes are 6 hours ER (*n* = 20 and 32) and PM (*n* = 14 and 23) and 10 hours ER (*n* = 20 and 24) and PM (*n* = 14 and 19). Two-sided unpaired *t*-test was used with *P* values of: 6 hours ER (<0.0001), 6 hours PM (0.4385), 10 hours ER (<0.0001) and 10 hours PM (<0.0001). **c**, Representative images of HT-1080 cells treated with DMSO, RSL3 (0.5 µM), FIN56 (10 µM) or FINO$_2$ (10 µM) for 2 hours and stained with C11 BODIPY (oxidized and reduced overlay), CellMask Deep Red and ER-Tracker Blue-White. **d**, Representative images of HT-1080 cells treated with DMSO, RSL3 (0.5 µM), FIN56 (10 µM) or FINO$_2$ (10 µM) for 5 hours and stained with C11 BODIPY (oxidized and reduced overlay), CellMask Deep Red and ER-Tracker Blue-White. For all panels, GraphPad Prism *P* value style of 0.1234 (NS), 0.0332 (*), 0.0021 (**), 0.0002 (***) and <0.0001 (****) was used. NS, not significant.

subcellular dynamics of this form of cell death and to provide important information for future development of ferroptosis-modulating drugs.

Online content
Any methods, additional references, Nature Portfolio reporting summaries, source data, extended data, supplementary information, acknowledgements, peer review information; details of author contributions

and competing interests; and statements of data and code availability are available at https://doi.org/10.1038/s41589-022-01249-3.

References
1. Stockwell, B. R. Ferroptosis turns 10: emerging mechanisms, physiological functions, and therapeutic applications. *Cell* **185**, 2401–2421 (2022).

2. Stockwell, B. R., Jiang, X. & Gu, W. Emerging mechanisms and disease relevance of ferroptosis. *Trends Cell Biol.* **30**, 478–490 (2020).

3. Su, Y. et al. Ferroptosis, a novel pharmacological mechanism of anti-cancer drugs. *Cancer Lett.* **483**, 127–136 (2020).

4. Reichert, C. O. et al. Ferroptosis mechanisms involved in neurodegenerative diseases. *Int. J. Mol. Sci.* **21**, 8765 (2020).

5. Ye, L. F. et al. Radiation-Induced lipid peroxidation triggers ferroptosis and synergizes with ferroptosis inducers. *ACS Chem. Biol.* **15**, 469–484 (2020).

6. Zhang, Y. et al. Imidazole ketone erastin induces ferroptosis and slows tumor growth in a mouse lymphoma model. *Cell Chem. Biol.* **26**, 623–633 (2019).

7. Badgley, M. A. et al. Cysteine depletion induces pancreatic tumor ferroptosis in mice. *Science* **368**, 85–89 (2020).

8. Louandre, C. et al. Iron-dependent cell death of hepatocellular carcinoma cells exposed to sorafenib. *Int. J. Cancer* **133**, 1732–1742 (2013).

9. Lachaier, E. et al. Sorafenib induces ferroptosis in human cancer cell lines originating from different solid tumors. *Anticancer Res.* **34**, 6417–6422 (2014).

10. Wang, Q. et al. GSTZ1 sensitizes hepatocellular carcinoma cells to sorafenib-induced ferroptosis via inhibition of NRF2/GPX4 axis. *Cell Death Dis.* **12**, 426 (2021).

11. Eling, N., Reuter, L., Hazin, J., Hamacher-Brady, A. & Brady, N. R. Identification of artesunate as a specific activator of ferroptosis in pancreatic cancer cells. *Oncoscience* **2**, 517–532 (2015).

12. Friedmann Angeli, J. P. et al. Inactivation of the ferroptosis regulator Gpx4 triggers acute renal failure in mice. *Nat. Cell Biol.* **16**, 1180–1191 (2014).

13. Li, Q. et al. Inhibition of neuronal ferroptosis protects hemorrhagic brain. *JCI Insight* **2**, e90777 (2017).

14. Liu, P. et al. Ferrostatin-1 alleviates lipopolysaccharide-induced acute lung injury via inhibiting ferroptosis. *Cell. Mol. Biol. Lett.* **25**, 10 (2020).

15. Feng, Y., Madungwe, N. B., Imam Aliagan, A. D., Tombo, N. & Bopassa, J. C. Liproxstatin-1 protects the mouse myocardium against ischemia/reperfusion injury by decreasing VDAC1 levels and restoring GPX4 levels. *Biochem. Biophys. Res. Commun.* **520**, 606–611 (2019).

16. Cao, Y. et al. Selective ferroptosis inhibitor liproxstatin-1 attenuates neurological deficits and neuroinflammation after subarachnoid hemorrhage. *Neurosci. Bull.* **37**, 535–549 (2021).

17. Hatami, A. et al. Deuterium-reinforced linoleic acid lowers lipid peroxidation and mitigates cognitive impairment in the Q140 knock in mouse model of Huntington's disease. *FEBS J.* **285**, 3002–3012 (2018).

18. Elharram, A. et al. Deuterium-reinforced polyunsaturated fatty acids improve cognition in a mouse model of sporadic Alzheimer's disease. *FEBS J.* **284**, 4083–4095 (2017).

19. Dixon, S. J. et al. Ferroptosis: an iron-dependent form of nonapoptotic cell death. *Cell* **149**, 1060–1072 (2012).

20. Kagan, V. E. et al. Oxidized arachidonic and adrenic PEs navigate cells to ferroptosis. *Nat. Chem. Biol.* **13**, 81–90 (2017).

21. Yang, W. S. et al. Peroxidation of polyunsaturated fatty acids by lipoxygenases drives ferroptosis. *Proc. Natl Acad. Sci. USA* **113**, E4966–E4975 (2016).

22. Yang, W. S. et al. Regulation of ferroptotic cancer cell death by GPX4. *Cell* **156**, 317–331 (2014).

23. Shimada, K. et al. Global survey of cell death mechanisms reveals metabolic regulation of ferroptosis. *Nat. Chem. Biol.* **12**, 497–503 (2016).

24. Gaschler, M. M. et al. FINO$_2$ initiates ferroptosis through GPX4 inactivation and iron oxidation. *Nat. Chem. Biol.* **14**, 507–515 (2018).

25. Wenzel, S. E. et al. PEBP1 wardens ferroptosis by enabling lipoxygenase generation of lipid death signals. *Cell* **171**, 628–641 (2017).

26. Doll, S. et al. ACSL4 dictates ferroptosis sensitivity by shaping cellular lipid composition. *Nat. Chem. Biol.* **13**, 91–98 (2017).

27. Gaschler, M. M. et al. Determination of the subcellular localization and mechanism of action of ferrostatins in suppressing ferroptosis. *ACS Chem. Biol.* **13**, 1013–1020 (2018).

28. Gao, M. et al. Role of mitochondria in ferroptosis. *Mol. Cell* **73**, 354–363 (2019).

29. Mao, C. et al. DHODH-mediated ferroptosis defence is a targetable vulnerability in cancer. *Nature* **593**, 586–590 (2021).

30. Magtanong, L. et al. Exogenous monounsaturated fatty acids promote a ferroptosis-resistant cell state. *Cell Chem. Biol.* **26**, 420–432 (2019).

31. Bersuker, K. et al. The CoQ oxidoreductase FSP1 acts parallel to GPX4 to inhibit ferroptosis. *Nature* **575**, 688–692 (2019).

32. Doll, S. et al. FSP1 is a glutathione-independent ferroptosis suppressor. *Nature* **575**, 693–698 (2019).

33. Shen, Y., Hu, F. & Min, W. Raman imaging of small biomolecules. *Annu. Rev. Biophys.* **48**, 347–369 (2019).

34. Hu, F., Shi, L. & Min, W. Biological imaging of chemical bonds by stimulated Raman scattering microscopy. *Nat. Methods* **16**, 830–842 (2019).

35. Hill, S. et al. Small amounts of isotope-reinforced polyunsaturated fatty acids suppress lipid autoxidation. *Free Radic. Biol. Med.* **53**, 893–906 (2012).

36. Firsov, A. M. et al. Threshold protective effect of deuterated polyunsaturated fatty acids on peroxidation of lipid bilayers. *FEBS J.* **286**, 2099–2117 (2019).

37. Shah, R., Shchepinov, M. S. & Pratt, D. A. Resolving the role of lipoxygenases in the initiation and execution of ferroptosis. *ACS Cent. Sci.* **4**, 387–396 (2018).

38. Raefsky, S. M. et al. Deuterated polyunsaturated fatty acids reduce brain lipid peroxidation and hippocampal amyloid β-peptide levels, without discernable behavioral effects in an APP/PS1 mutant transgenic mouse model of Alzheimer's disease. *Neurobiol. Aging* **66**, 165–176 (2018).

39. Zou, Y. et al. Plasticity of ether lipids promotes ferroptosis susceptibility and evasion. *Nature* **585**, 603–608 (2020).

40. Cui, W., Liu, D., Gu, W. & Chu, B. Peroxisome-driven ether-linked phospholipids biosynthesis is essential for ferroptosis. *Cell Death Differ.* **28**, 2536–2551 (2021).

41. Gijón, M. A., Riekhof, W. R., Zarini, S., Murphy, R. C. & Voelker, D. R. Lysophospholipid acyltransferases and arachidonate recycling in human neutrophils. *J. Biol. Chem.* **283**, 30235–30245 (2008).

42. Jiménez-López, J. M., Ríos-Marco, P., Marco, C., Segovia, J. L. & Carrasco, M. P. Alterations in the homeostasis of phospholipids and cholesterol by antitumor alkylphospholipids. *Lipids Health Dis.* **9**, 33 (2010).

43. Neve, E. P. A., Boyer, C. S. & Moldéus, P. *N*-ethyl maleimide stimulates arachidonic acid release through activation of the signal-responsive phospholipase A2 in endothelial cells. *Biochem. Pharmacol.* **49**, 57–63 (1995).

44. Loi, M., Fregno, I., Guerra, C. & Molinari, M. Eat it right: ER-phagy and recovER-phagy. *Biochem. Soc. Trans.* **46**, 699–706 (2018).

45. Morishita, H. et al. Organelle degradation in the lens by PLAAT phospholipases. *Nature* **592**, 634–638 (2021).

46. Liu, L. et al. Mitochondrial outer-membrane protein FUNDC1 mediates hypoxia-induced mitophagy in mammalian cells. *Nat. Cell Biol.* **14**, 177–185 (2012).

47. Dierge, E. et al. Peroxidation of n-3 and n-6 polyunsaturated fatty acids in the acidic tumor environment leads to ferroptosis-mediated anticancer effects. *Cell Metab.* **33**, 1701–1715 (2021).

48. Dixon, S. J. et al. Pharmacological inhibition of cystine-glutamate exchange induces endoplasmic reticulum stress and ferroptosis. *eLife* **3**, e02523 (2014).

49. Lee, Y. S. et al. Ferroptotic agent-induced endoplasmic reticulum stress response plays a pivotal role in the autophagic process outcome. *J. Cell. Physiol.* **235**, 6767–6778 (2020).

50. Riegman, M. et al. Ferroptosis occurs through an osmotic mechanism and propagates independently of cell rupture. *Nat. Cell Biol.* **22**, 1042–1048 (2020).

Methods

Cell lines

HT-1080 (human (*Homo sapiens*) male fibrosarcoma), PANC-1 (human (*H. sapiens*) male pancreatic epithelial fibrosarcoma), HEK293T (human (*H. sapiens*) male fibrosarcoma), N27 (rat (*Rattus norvegicus*) dopaminergic neural cell line) and HT22 (mouse (*Mus musculus*) hippocampal neuronal cell line) were obtained from the American Type Culture Collection (https://www.atcc.org/). HT-1080, HEK293T and HT-22 cells were cultured in DMEM with 10% FBS, 1% non-essential amino acids and 1% penicillin–streptomycin (P–S). PANC-1 cells were cultured in DMEM with 10% FBS and 1% P–S. N27 cells were cultured in RPMI medium with 10% FBS, 2 mM L-glutamine and 1% P–S. All cells were cultured at 37 °C and 5% CO_2.

Chemicals and reagents

Reagents used in this study include: arachidonic acid-d_6 (Retrotope), eicosapentaenoic acid-d_8 (Retrotope), docosahexaenoic acid-d_{10} (Retrotope), erastin (Cayman Chemical), IKE (Stockwell laboratory), RSL3 (Stockwell laboratory), FIN56 (gift of Rachid Skouta), $FINO_2$ (Woerpel laboratory), BQR (Cayman Chemical), PF-06424439 (Cayman Chemical), A922500 (Cayman Chemical), arachidonic acid-d_{11} (Cayman Chemical), docosahexaenoic acid-d_5 (Cayman Chemical), oleic acid-d_{17} (Cayman Chemical), palmitoleic acid-d_{13} (Cayman Chemical), myristic acid-d_{27} (Sigma-Aldrich), cholesterol-d_6 (Sigma-Aldrich), Thimerosal Ready Made Solution (Sigma-Aldrich), miltefisone (Cayman Chemical), *N*-ethylmaleimide (Sigma-Aldrich), LysoTracker Green DND-26 (Invitrogen), LysoTracker Red DND-99 (Invitrogen), Nile Red (Invitrogen), ER-Tracker Red (Invitrogen), ER-Tracker Green (Invitrogen), ER-Tracker Blue-White DPX (Invitrogen), BODIPY TR Ceramide complexed to BSA (Invitrogen), MitoTracker Red CMXRos (Invitrogen), Hoechst 33342 (Invitrogen), BODIPY 581/591 C11 (Invitrogen), CellMask Deep Red (Invitrogen) and FM 4-64 (Invitrogen).

Dose–response assays

Cells were seeded in a 384-well plate at 1,500 cells per well. In experiments using D-PUFAs, cells were treated at the time of seeding. After 24-hour incubation at 37 °C/5% CO_2, cells were treated with compounds of interest and incubated for a further 24 hours at 37 °C/5% CO_2. Cell viability was evaluated with CellTiter-Glo (Promega), and results were worked up in GraphPad Prism. All treatments were performed in triplicate.

SRS imaging and analysis

Cells were seeded on 12-mm circular cover glasses (Thermo Fisher Scientific) in a 24-well plate at 50,000 cells per well. In experiments using deuterated fatty acids, cells were treated at the time of seeding and incubated for 24 hours at 37 °C/5% CO_2. In experiments with $FINO_2$-2, cells were treated after overnight incubation at 37 °C/5% CO_2. All treatments were performed in duplicate. SRS imaging was performed with a system coupling two spatially and temporally overlapped laser beams from an integrated laser source (picoEmerald, Applied Physics & Electronics) into a commercial confocal laser scanning microscope (FV1200MPE, Olympus). One of the laser beams for SRS is a tunable pump beam (720–990 nm, 5–6 ps); the other is a Stokes beam with fixed wavelength (1,064 nm, 6 ps, intensity modulated at 8 MHz). Both are at 80-MHz repetition rate. The two beams are focused onto the cell samples through a ×25 water objective (XLPlan N, 1.05 NA MP, Olympus), and the transmitted beams are then collected by a high-NA oil condenser lens (1.4 NA, Olympus) for detection. A high O.D. band-pass filter (890/220 CARS, Chroma Technology) is used to block the Stokes beam and leave only the pump beam to be collected by a silicon photodiode (FDS1010, Thorlabs) with a DC voltage of 64 V. The output current of the photodiode was terminated by 50 Ω and demodulated with a high-frequency lock-in amplifier (HF2LI, Zurich Instruments) at 8-MHz frequency. The stimulated Raman loss signal at each pixel is sent to the analog interface box (FV10-ANALOG, Olympus) of the microscope to generate the image. All images (512 × 512 pixels) are acquired with 30-μs time constant at the lock-in amplifier and 100-μs pixel dwell time. The on-sample power for SRS imaging was 80 mW for pump beam and 120 mW for Stokes beam.

For evaluation of incorporation of D-FA into ER and PM, cells treated with 20 μM D-FA were incubated with 1 μM ER-Tracker Green (Invitrogen) in HBSS for 15 minutes at 37 °C and with 10 μg ml^{-1} FM 4-64 (Invitrogen) in HBSS for 5 minutes at room temperature for ER and PM labeling. The CH_2 on-resonance channel was acquired at 2,850 cm^{-1}, and the CD on-resonance channel was acquired at 2,105 cm^{-1}. Off-resonance channels were acquired at 1,900 cm^{-1} and were used for subtraction from the on-resonance channel to obtain the pure SRS signal. The PM and ER regions in cells were segmented on the CH_2 on-resonance channel with reference to the corresponding PM and ER fluorescence images using MATLAB R2020a. Concentrated lipid droplets gave saturated SRS signals and were removed from segmented regions. The pure SRS signals for CD and CH_2 were obtained by subtracting the on-resonance image with the off-resonance image at the same condition.

Confocal fluorescence imaging

Cells were seeded in four-well coverglass chambers (Nunc Lab-Tek) at 150,000 cells per well or eight-well cover glass chambers at 50,000 cells per well. In experiments using fatty acids, cells were treated at the time of seeding and incubated for 24 hours at 37 °C/5% CO_2. In experiments with $FINO_2$ analogs and FINs, cells were treated after overnight incubation at 37 °C/5% CO_2. After relevant staining as described below, cells were placed in HBSS, and images were taken using Zeiss LSM 700 and 800 confocal microscopes with Zeiss ZEN Blue 2.1 software and then worked up in Fiji/CellProfiler[51,52]. For quantification of images, CellProfiler was used. For ER versus PM quantification, ER and PM of each cell were identified as objects using their respective stains. The ratio of the median signal for C11 BODIPY oxidized and reduced channels were then determined for every cell within the identified ER and PM regions, and these were plotted. For ER versus mitochondria quantification, co-localization of C11 BODIPY was used instead owing to the proximity of the ER and mitochondria stains and the small size of the mitochondria making object identification too difficult. The co-localization metrics were measured only for pixels above a certain threshold, which was set as 20% of the maximum intensity of the image to eliminate the background. The Manders coefficient was used to represent the correlation of pixel intensity between C11 BODIPY oxidized and either the ER stain or the mitochondrial stain. For quantification of ER size, objects were identified using adaptive Otsu two-class thresholding, and their size properties were calculated and exported with at least six images used for each sample, resulting in the sample sizes of number of cells defined as *n*.

Fluorescent staining of live cells

Fluorescent labels were used according to the manufacturer's instructions. LysoTracker Green DND-26 (Invitrogen) and LysoTracker Red DND-99 (Invitrogen) were diluted to 50 nM in HBSS and incubated for 30 minutes at 37 °C. Nile Red (Invitrogen) was diluted to 1 μg ml^{-1} in HBSS and incubated for 5 minutes at room temperature. ER-Tracker Green, ER-Tracker Red and ER-Tracker Blue-White (Invitrogen) were diluted to 1 μM in HBSS and incubated for 20 minutes at 37 °C. Golgi stain BODIPY TR Ceramide complexed to BSA (Invitrogen) was diluted to 5 μM and incubated at 37 °C for 30 minutes. MitoTracker Red CMXRos (Invitrogen) was diluted to 50 nM in HBSS and incubated at 30 minutes. Hoechst 33342 was diluted to 1 μg ml^{-1} and incubated for 5 minutes at room temperature. BODIPY 581/591 C11 (Invitrogen) was diluted to 10 μM and incubated for 10 minutes at 37 °C. CellMask Deep Red Plasma Membrane Stain (Invitrogen) was diluted to 5 μg ml^{-1} in HBSS and incubated for 10 minutes at 37 °C.

Immunofluorescence imaging

HT-1080 cells were seeded on eight-well chambered slides (Thermo Fisher Scientific) at 0.05 million cells per well and incubated overnight. Cells were washed with PBS twice and fixed with 4% paraformaldehyde for 30 minutes at room temperature in the dark. Cells were than permeabilized by three washes with PBST (PBS with 0.1% Triton X-100). Cells were blocked with 5% normal goat serum in PBST for 1 hour at room temperature. Cells were stained with mouse anti-ACSL4 antibody (Invitrogen) 1:250 and rabbit anti-calnexin antibody (Invitrogen) 1:333 overnight at 4 °C. Cells were washed three times with PBST and stained with Alexa Fluor 594-conjugated anti-mouse (Invitrogen) 1:500 and Alexa Fluor 488-conjugated anti-rabbit antibody (Invitrogen) 1:500 at room temperature for 1 hour. Cells were washed three times with PBST. Slides were slightly dried, one drop of antifade mountant with DAPI (Invitrogen) added, and covered with cover glass. Slides were dried overnight and imaged using a Zeiss LSM 800 confocal microscope.

Lipidomics with high-resolution mass spectrometry

HT-1080 cells were seeded at 5 million cells per 10-cm dish in triplicate, with either ethanol as vehicle or 20 μM PUFA, and incubated for 24 hours. Cells were harvested, and lipids were isolated and analyzed as previously described[6,53]. In brief, cells were homogenized with a microtip sonicator in 250 μl of ice-cold methanol with 0.01% butylated hydroxyltoluene (BHT) and then transferred to glass tubes containing 850 μl of cold methyl-tert-butyl ether (MTBE) and vortexed for 30 seconds. Samples were then incubated on a shaker at 4 °C for 2 hours. Then, 200 μl of cold water was added, and they were incubated on ice for 20 minutes before centrifugation at 3,000 r.p.m. for 20 minutes at 4 °C. The organic layer was collected and dried under a stream of nitrogen gas on ice. Next, the samples were reconstituted in a solution of 2-propanol/acetonitrile/water (4:3:1, v/v/v) containing a splashlipidomix standard (Avanti Polar Lipids). Ultra-performance liquid chromatography was then performed at 55 °C on an Acquity UPLC HSS T3 Column, (1.8 μm, 2.1 mm × 100 mm) over a 20-minute gradient elution. Mobile phase A was acetonitrile/water (60:40, v/v); mobile phase B was 2-propanol/acetonitrile/water (85:10:5, v/v/v), both containing 10 mM ammonium acetate and 0.1% acetic acid. After injection, the gradient was held at 40% mobile phase B for 2 minutes. For the next 12 minutes, the gradient was ramped in a linear fashion to 100% B and held at this composition for 3 minutes. The eluent composition returned to the initial condition in 1 minute, and the column was re-equilibrated for an additional 1 minute before the next injection was conducted. The flow rate was 0.4 ml min^{-1}, and injection volumes were 6 μl. The SYNAPT G2 mass spectrometer (Waters) was operated in both positive and negative electrospray ionization (ESI) modes. All raw data files were converted to netCDF format using the DataBridge tool implemented in MassLynx software (Waters, version 4.1). They were then subjected to peak-picking, retention time alignment and grouping using the XCMS package (version 3.2.0) in the R (version 3.4.4) environment[54,55]. After retention time alignment and filling missing peaks, an output data frame was generated containing the list of time-aligned detected features (m/z and retention time) and the relative signal intensity (area of the chromatographic peak) in each sample. All the extracted features were normalized to measured protein concentrations measured by BCA assay (Pierce). Structural assignment and structural characterization of significant lipid features were initially obtained by searching monoisotopic masses against the available online databases, such as METLIN, Lipid MAPS and HMDB, with a mass tolerance of 5 ppm and by confirming fragmentation patterns of HDMSE data in MS^E data viewer (version 1.3, Waters).

Isolation of mitochondrial and ER fractions

Samples were subject to fractionation using commercially available mitochondrial isolation (Thermo Fisher Scientific, 89874) and ER isolation (MilliporeSigma, ER0100-1KT) kits for each respective fraction.

In brief, for mitochondrial fractionation, cells were spun down at 850g for 2 minutes, resuspended in 1.6 ml of reagent A, vortexed for 5 seconds and incubated on ice for 2 minutes. Cells were homogenized in a 7-ml dounce homogenizer (Bellco Glass); 1.6 ml of reagent C was added; and suspension was centrifuged at 700g for 10 minutes at 4 °C. Supernatant was then transferred to new tubes and spun down at 3,500g for 15 minutes at 4 °C. After spin-down, supernatant was discarded and pellet resuspended in 500 μl of reagent C and centrifuged at 12,000g for 5 minutes at 4 °C. The resulting mitochondrial fraction pellet was isolated, flash frozen and maintained at −80 °C until use.

For ER fractionation, cells were centrifuged at 600g for 5 minutes at 4 °C and supernatant discarded. Cells were washed with ten volumes of PBS and pelleted again under identical conditions. Cells were resuspended in 3 ml of hypotonic extraction buffer and incubated on ice for 20 minutes. Cells were then centrifuged at 600g for 5 minutes at 4 °C; the supernatant was discarded; and the pellet was resuspended in 2 ml of isotonic extraction buffer. Suspension was homogenized in 7 ml of dounce homogenizer, and homogenate was centrifuged at 1,000g for 10 minutes at 4 °C.

The central supernatant above the pellet but below the thin lipid layer on top was isolated by slowly puncturing the top lipid layer, and 1.5 ml of the central supernatant layer was transferred to a new tube and centrifuged again at 12,000g for 15 minutes at 4 °C. Again, 1 ml of the central layer was transferred to a new tube and then to a flat-bottom 250-ml glass beaker with a stir bar inside. Next, 8 mM calcium chloride solution was added dropwise while stirring to the beaker on ice, and, once added, the solution was stirred for an additional 15 minutes. Solution was then subject to centrifugation at 8,000g for 10 minutes at 4 °C; the supernatant was siphoned off; and the pellet was flash frozen and stored at −80 °C until use.

Cloning of overexpression retrovirus plasmids

NEBuilder HiFi DNA Assembly Cloning Kit (New England Biolabs) was used to clone inserts of interest into retroviral expression plasmid pMRX-IP-GFP (gift of Noboru Mizushima)[45]. Gibson assembly primers for genes of interest were designed (Supplementary Table 1), and inserts were amplified by polymerase chain reaction (PCR) using Phusion High-Fidelity Polymerase (New England Biolabs) on a T100 Thermal Cycler (Bio-Rad). For ACSL4 and FUNDC1, insert amplification was performed with pCMV-Entry-ACSL4 (OriGene) and pcDNA4/TO/Myc-His-FUNDC1 (gift of Quan Chen), respectively, and pMRX-IP-GFP-Plaat3 (PLA2G16) was then digested using BamHI and XhoI in CutSmart Buffer (New England Biolabs). To introduce the cytochrome b5 sequence into pMRX-IP-GFP-PLA2G16, two inserts were made using long primers to introduce the new sequence in, resulting in a three-piece assembly that required digesting the vector with BamHI and BsiWI. For PLA2G16-cyb5, the pMRX-IP-GFP-PLA2G16 was used as template and vector for digestion. For FUNDC1-cyb5, the pMRX-IP-GFP-FUNDC1 was used as template, and the same primers as PLA2G16 were used with the exception of FUNDC1-cyb5 R1 substituted for PLA2G16-cyb5 R1. To make the pMRX-IP-GFP control plasmid, the three GFP primers in the table were used along with PLA2G16-cyb5 R2 to amplify the two inserts from pMRX-IP-GFP-PLA2G16, and vector was cut with HindIII and BsiWI. To make pMRX-IP-GFP-cyb5, pMRX-IP-GFP-PLA2G16-cyb5 was amplified with GFP-cyb5 F and PLA2G16-cyb5 R2, and pMRX-IP-GFP was digested with BamHI and BsiWI. To make the N-terminus cyb5-tagged FUNDC1 plasmid, the FUNDC1-cyb5 primers were used with GFP F1 and PLA2G16-cyb5 R2, with pMRX-IP-GFP-FUNDC1 and pMRX-IP-GFP-PLA2G16-cyb5 as templates and with pMRX-IP-GFP digested with HindIII and BsiWI. All PCR and digestion products were gel purified using the Zymoclean Gel Recovery Kit. The HiFi kit was then used according to the manufacturer's instructions, and the reaction was incubated at 50 °C for 1 hour. The reactions were then transformed into Stable (New England Biolabs) or Stbl3 (Invitrogen) cells and plated on LB/agar plates. Resulting colonies were grown up with QIAprep Spin Miniprep Kit (Qiagen) and sent to GENEWIZ

for Sanger sequencing. The primers used for these experiments are detailed in Supplementary Table 1.

Generation of overexpression and stable knockdown cell lines by viral infection

For overexpression cell lines, genes were inserted into pMRX-IPU-GFP as described above. For this plasmid, the pUMVC gag-pol plasmid and pVSV-G envelope plasmid were used[56]. For knockdown cell lines, glycerol stocks of Mission shRNA knockdown sequences in pLKO.1-puro were purchased from Sigma-Aldrich (Supplementary Table 3). For this plasmid, the psPAX2 gag-pol plasmid and pVSV-G envelope plasmid were used.

To produce virus, 400,000 HEK293T cells per well were seeded in 2.5 ml in six-well plates and incubated overnight at 37 °C/5% CO_2. To 250 μl of OptiMEM (Gibco), 1.25 μg of knockdown or overexpression plasmid, 1.25 μg of gag-pol plasmid and 0.156 μg of VSV-G plasmid were added. Next, 8 μl of TransIT LT1 (Mirus) was added, and this solution was mixed and incubated at room temperature for 15–30 minutes. The solution was then added dropwise to HEK293T cells and incubated overnight at 37 °C/5% CO_2. Transfection medium was replaced with 5 μl of fresh medium, and cells were incubated at 32 °C/5% CO_2 for 24 hours. Viral supernatant was harvested; 250 μl of 1 M HEPES buffer (Gibco) was added; and the supernatant was filtered through a 0.45-μm syringe filter. Aliquots were then either frozen and stored at −80 °C or applied directly to cells of interest.

To infect cells, viral supernatant with a 1:2,000 dilution of 10 mg ml^{-1} polybrene (Santa Cruz Biotechnology) was applied to cells of interest seeded in six-well plates and incubated overnight at 37 °C/5% CO_2. Fresh media was then applied, and cells were incubated for 24 hours. Selection media containing 1 μg ml^{-1} puromycin was then added, and selection/expansion took place. Knockdowns/overexpressions were confirmed by qPCR or western blot as described below.

qPCR

Cells were harvested, washed with PBS and lysed using QIAshredder (Qiagen). RNEasy kit (Qiagen) was used to isolate RNA, and RT–PCR was performed using MultiScribe Reverse Transcriptase (Invitrogen) on a T100 Thermal Cycler (Bio-Rad). qPCR reactions were then performed in triplicate using Power SYBR Green PCR Master Mix (Applied Biosystems) on a ViiA 7 Real-Time PCR instrument (Thermo Fisher Scientific). TBP was used as an internal reference. Differences in mRNA levels compared with TBP were computed between vehicle and experimental groups using the ΔΔCt method. The primers used in the study are detailed in Supplementary Table 2.

Western blotting

Cells were harvested, washed with PBS and incubated in RIPA buffer containing cOmplete, Mini Protease Inhibitor Tablets (Sigma-Aldrich) on ice for 30 minutes. These were then centrifuged at 14,000g for 15 minutes at 4 °C. Protein concentrations of supernatants were determined using the BCA Protein Assay Kit (Pierce), and concentrations were normalized and diluted with 4× SDS running buffer (Invitrogen). NuPAGE Novex 4–12% Bis-Tris Midi Protein Gel (Invitrogen) was loaded at run in MES buffer (Invitrogen) for 30 minutes at 200 V. Proteins were then transferred to PVDF membrane (Invitrogen) using the iBlot2 machine. Membrane was washed in PBS and then blocked overnight at 4 °C in Intercept Blocking Buffer (LI-COR). Membrane was then incubated overnight at 4 °C with primary antibodies in a 1:1 solution of blocking buffer and PBST. Membrane was then washed three times with PBST, incubated for 1 hour at room temperature with secondary antibodies in 1:1 solution of blocking buffer and PBST and then washed three more times with PBST. It was then imaged with the ChemiDoc MP Imaging System (Bio-Rad). Antibodies used included mouse monoclonal anti-ACSL4 (F-4) (Santa Cruz Biotechnology) 1:500; rabbit monoclonal anti-pan-actin (D18C11) (Cell Signaling Technology) 1:1,000; mouse monoclonal anti-β-actin (8H10D10) (Cell Signaling Technology) 1:1,000; rabbit monoclonal anti-cytochrome C (D18C7) (Cell Signaling Technology) 1:1,000; rabbit monoclonal anti-PDI (C81H6) (Cell Signaling Technology) 1:1,000; IRDye goat anti-mouse 680 1:5,000; and IRDye goat anti-rabbit 800 (LI-COR) 1:5,000.

For synthetic methods, see Supplementary Note.

Statistical analysis and reproducibility

Statistical analysis was performed in Prism using ANOVA with multiple comparison control or two-sided unpaired t-test with 95% confidence. GraphPad Prism P value style of 0.1234 (NS), 0.0332 (*), 0.0021 (**), 0.0002 (***) and <0.0001 (****) was used. All SRS and confocal fluorescence images are representative. SRS imaging was performed with at least two independent experiments with at least three images. Confocal fluorescence imaging was performed at least twice for each FINO$_2$ analog with a minimum of three images per experiment. Immunofluorescence imaging was performed twice with a minimum of three images per experiment. C11 BODIPY imaging of ER and PM was repeated three times with at least five images per condition. C11 BODIPY imaging of ER and mitochondria was repeated twice with at least two images per condition.

Reporting summary

Further information on research design is available in the Nature Portfolio Reporting Summary linked to this article.

Data availability

Lipidomics data are available at Academic Commons at https://doi.org/10.7916/rphv-v394. All other data, including statistical data and blots, are available as Source Data and at https://doi.org/10.7916/hggm-7r90. Source data are provided with this paper.

References

51. Schindelin, J. et al. Fiji: an open-source platform for biological-image analysis. *Nat. Methods* **9**, 676–682 (2012).
52. McQuin, C. et al. CellProfiler 3.0: next-generation image processing for biology. *PLoS Biol.* **16**, 1–17 (2018).
53. Kraft, V. A. N. et al. GTP cyclohydrolase 1/tetrahydrobiopterin counteract ferroptosis through lipid remodeling. *ACS Cent. Sci.* **6**, 41–53 (2020).
54. Smith, C. A., Want, E. J., O'Maille, G., Abagyan, R. & Siuzdak, G. XCMS: processing mass spectrometry data for metabolite profiling using nonlinear peak alignment, matching, and identification. *Anal. Chem.* **78**, 779–787 (2006).
55. R Core Team. R: a language and environment for statistical computing (2014).
56. Stewart, S. A. et al. Lentivirus-delivered stable gene silencing by RNAi in primary cells. *RNA* **9**, 493–501 (2003).

Author contributions

A.N.K. performed all biochemical experiments with D-PUFAs. A.N.K. prepared D-PUFA samples for imaging, and F.H. and N.Q. performed SRS imaging. Relative quantification of D-PUFAs in membranes by SRS was done by N.Q. High-resolution SRS imaging samples for mitochondrial evaluation were prepared by T.H. and imaged by N.Q. Quantification of PUFA incorporation into knockdown cell lines by SRS imaging was done by F.H. A.N.K. and F.Z. designed the

Competing interests

Additional information
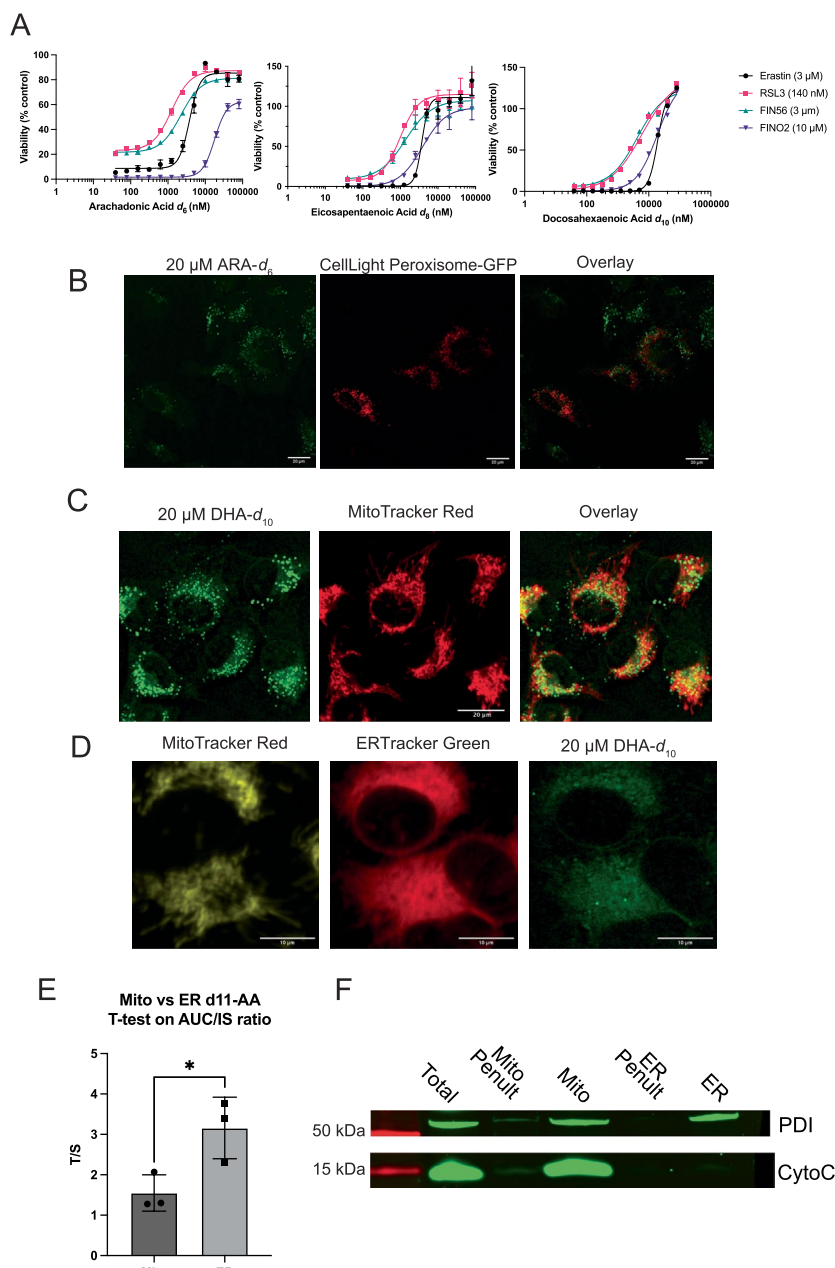
Extended Data Fig. 1 | Dose-response of D-PUFAs, peroxisome and mitochondrial staining of D-PUFA-treated cells, and mitochondrial/ER quantification of D-PUFAs. a. Dose-response curves of HT-1080 cells pre-treated with varying concentrations of D-PUFAs and then treated with FINs. Data are plotted as mean ± SEM, n=3 biologically independent samples. **b**. HT-1080 cells treated for 24 hours with 20 µM ARA-d_6 and CellLight Peroxisome-GFP, and imaged by fluorescence and SRS imaging. **c**. HT-1080 cells treated for 24 hours with 20 µM DHA-d_{10}, and then stained with MitoTracker Red CMXRos and imaged by fluorescence and SRS imaging. **d**. High resolution SRS imaging of HT-1080 cells treated for 24 hours with 20 µM DHA-d_{10} with DGAT inhibitors PF-06424439 (1 µM) and A922500 (1 µM), then stained with MitoTracker Red CMXRos and ERTracker Green and imaged by fluorescence and SRS imaging. **e**. Quantification of arachidonic acid-d_{11} in mitochondrial and ER fractions isolated from HT-1080 cells treated at 20 µM for 24 hours. Values determined by high resolution mass spectrometry and plotted as normalized to internal standard. Data are plotted as mean of three biological replicates ± SEM. **f**. Western blotting of mitochondrial and ER fractions stained for PDI as ER marker and Cytochrome C as mitochondrial marker, representative of four experiments. Results indicate no mitochondrial contamination of ER fraction, but indicate ER contamination of mitochondrial fraction.
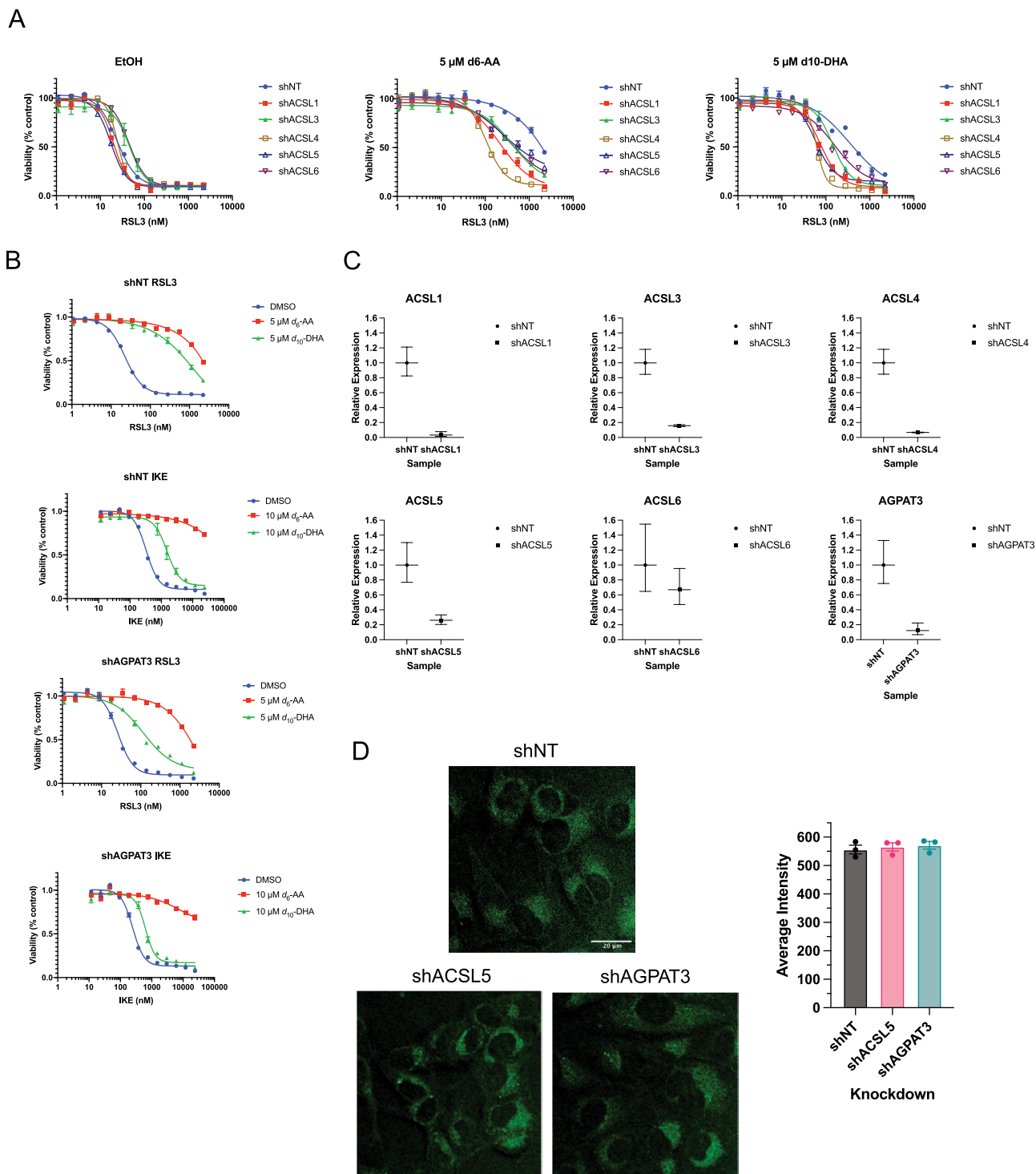
Extended Data Fig. 2 | Knockdown of PUFA-related genes shows some impact on D-PUFA potency, but no observable decrease in incorporation. a. Dose-response curves of stable non-targeting (NT) or ACSL knockdown HT-1080 cells pretreated with EtOH or D-PUFAs and then treated with RSL3. Data are represented as mean ± SEM, n=3. **b.** Dose-response curves of stable nontargeting (NT) or AGPAT3 knockdown HT-1080 cells pretreated with EtOH or D-PUFAs and then treated with RSL3 or IKE. Data are represented as mean ± SEM, n=3. **c.** qPCR data of stable shRNA knockdowns. Data are represented as mean of three technical replicates ± upper and lower limit of 95% confidence interval. **d.** SRS images of shNT, shACSL5, and shAGPAT3 HT-1080 cells treated with DHA-d_{10} (10 µM) (left), and quantification of their signal intensity (right), Data are plotted as mean ± SEM, n=3.
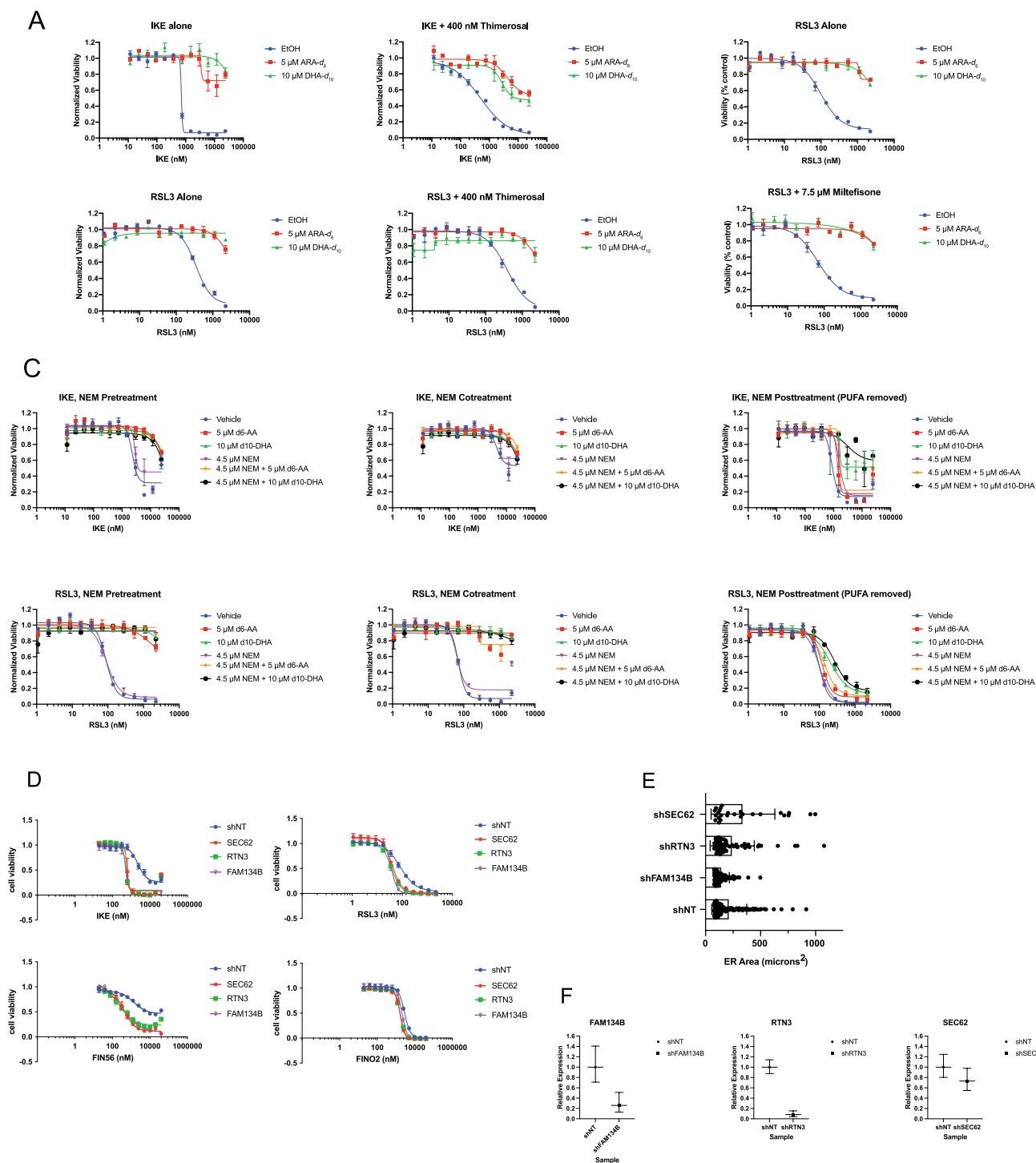
Extended Data Fig. 3 | Thimerosal, Miltefosine, and N-Ethyl Maleimide do not impact anti-ferroptotic potency of D-PUFAs, and knockdown of ER-phagy related genes SEC62, RTN3, and FAM134B did not result in apparently altered ER area. a. Dose-response curves of HT-1080 cells treated with vehicle (water) or 400 nM thimerosal, and subsequently treated with vehicle (EtOH) or PUFAs 4 hours later, followed by varying concentrations of IKE and RSL3 24 hours later. Data are represented as mean ± SEM, n=3. **b.** Dose-response curves of HT-1080 cells treated with vehicle (water) or 7.5 μM miltefosine, and subsequently treated with vehicle (EtOH) or PUFAs 4 hours later, followed by varying concentrations of RSL3 24 hours later. Data are represented as mean ± SEM, n=3. **c.** Dose-response curves of HT-1080 cells treated with D-PUFAs and either pretreated, cotreated, or post-treated with vehicle (EtOH) or 4.5 μM NME, and subsequently treated with

varying concentrations IKE and RSL3. In the post-treatment experiments, media containing PUFAs was removed before NME was added. Data are represented as mean ± SEM, n=3. **d.** Dose-response curves of stable shNT, shSEC62, shRTN3, and shFAM134B HT-1080 cells treated with varying doses of IKE, RSL3, FIN56, and FINO₂. Data are represented as mean ± SEM, n=3. **e.** ER area of ER-Phagy knockdown cell lines as compared to control. Cells were stained with ERTracker Blue-White, imaged with confocal microscopy, and their ER areas were measured using the CellProfiler software. Individual ER areas are shown for each cell, as well as the mean ± SD. Sample sizes (number of cells) are as follows: shNT n=123, shFAM134B n=98, shRTN3 n=60, shSEC62 n=26. **f.** qPCR analysis of knockdowns of ER-phagy genes in HT-1080 cells. Data are represented as mean of three technical replicates ± upper and lower limit of 95% confidence interval.
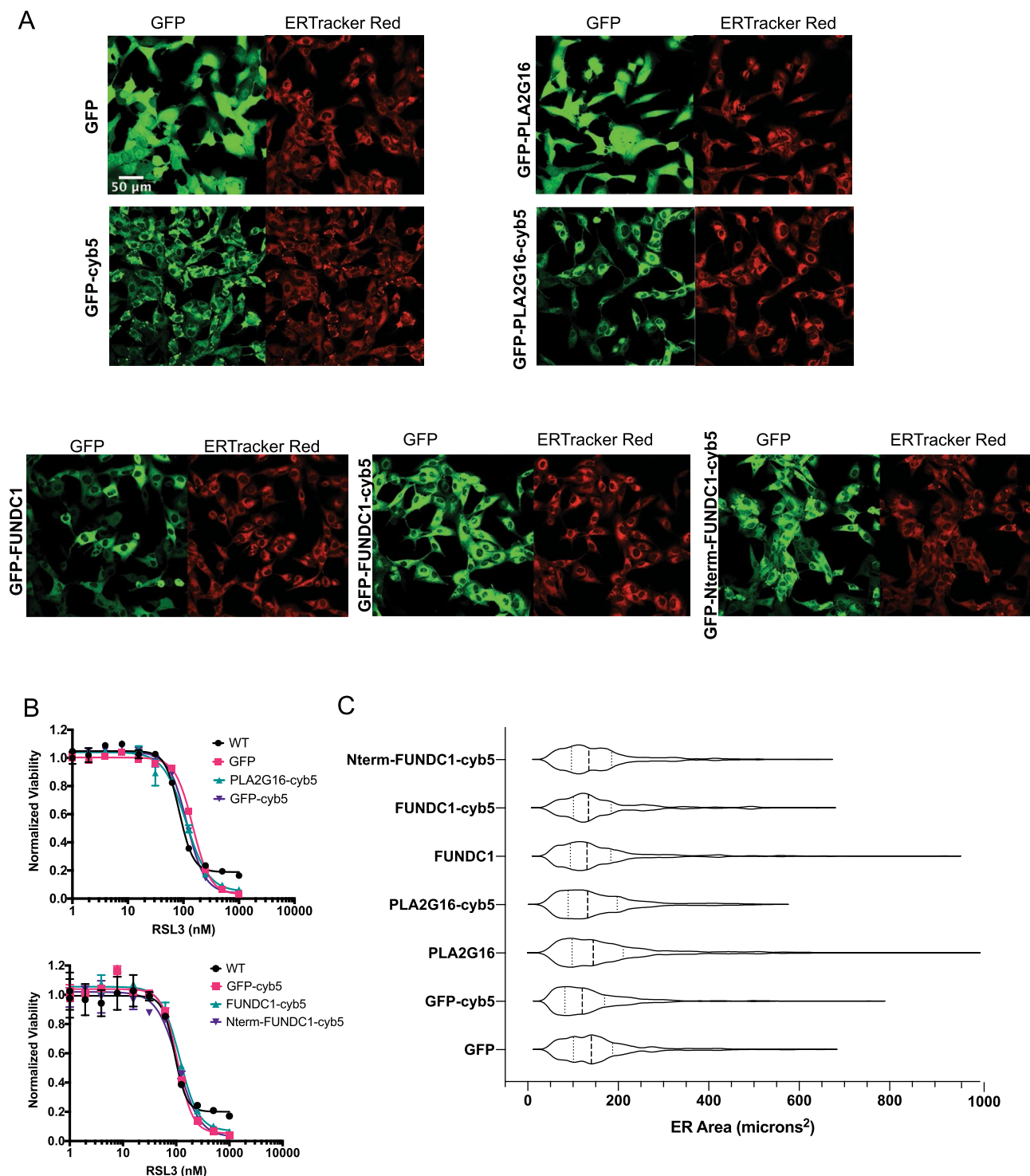
Extended Data Fig. 4 | Overexpression and targeting of organelle-phagy related genes did not result in apparently altered ER area. a. Confocal fluorescence images of HT-1080 cells overexpressing GFP, GFP-PLA2G16, GFP-FUNDC1 (as well as the cytoplasmic N-terminal FUNDC1 sequence), with and without C terminal-cytochrome b5 ER targeting signals, stained with ERTracker Red. GFP channels show protein distribution as all overexpressed proteins are tagged with GFP. Representative images of at least six images per sample are shown. **b.** Dose-response curves of overexpression cell lines with varying doses of RSL3. Data are represented as mean ± SEM, n=3 biologically independent samples. **c.** ER area overexpression cell lines as compared to control. Cells were stained with ERTracker Red, imaged with confocal microscopy, and their ER areas were measured using the CellProfiler software. Violin quartile plots are shown. Sample sizes (number of cells) are as follows: GFP n=358, GFP-cyb5 n=478, PLA2G16 n=353, PLA2G16-cyb5 n=292, FUNDC1 n=354, FUNDC1-cyb5 n=212, Nterm-FUNDC1-cyb5 n=399.
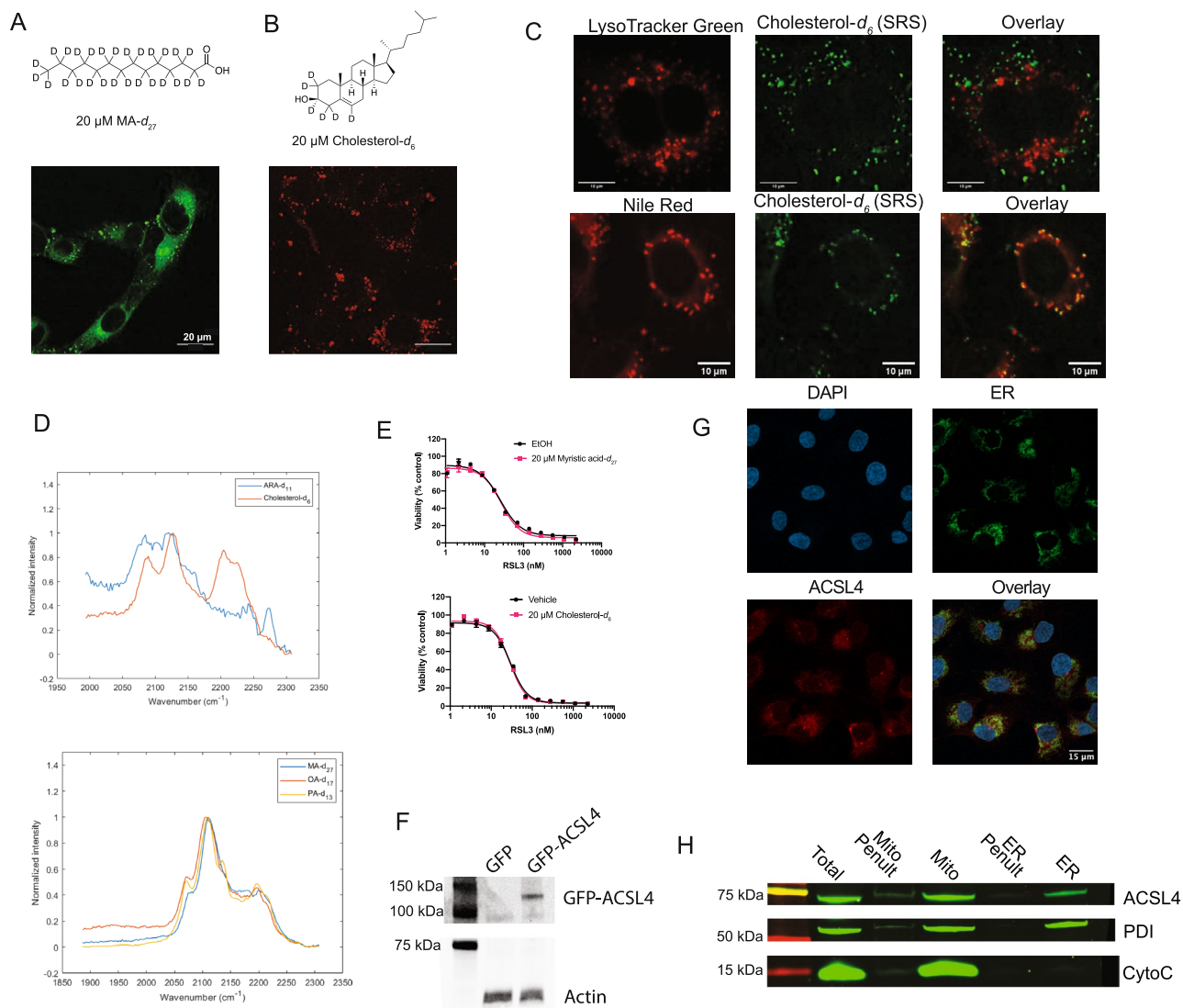
Extended Data Fig. 5 | Subcellular localization and effect on ferroptosis of myristic acid and cholesterol, overexpression and distribution of ACSL4.
**a**. Structure and SRS image of myristic acid-d_{27} (20 μM) in HT-1080 cells.
b. Structure and SRS image of cholesterol-d_6 (20 μM) in HT-1080 cells.
c. Fluorescence and confocal imaging of cholesterol-d_6 to evaluate its subcellular localization. **d**. Solution Raman spectra of the FAs and cholesterol used in these experiments. **e**. Dose-response curves of HT-1080 cells pretreated with either MA-d_{27} or cholesterol-d_6 (20 μM) followed by varying concentrations of RSL3. Data are represented as mean ± SEM, n=3. **f**. Western blot of HT-1080 cells overexpressing GFP (control) or GFP-ACSL4. ACSL4 antibody was used, with actin as a control. **g**. Immunofluorescence staining of HT-1080 cells labeled for ACSL4 (anti-ACSL4 antibody), ER (anti-calnexin antibody), and nucleus (DAPI). Individual channels and overlay is shown. **h**. Western blotting of mitochondrial and ER HT-1080 fractions stained for ACSL4 PDI (ER), and Cytochrome C (mitochondria), indicating presence in both fractions, representative of two experiments.
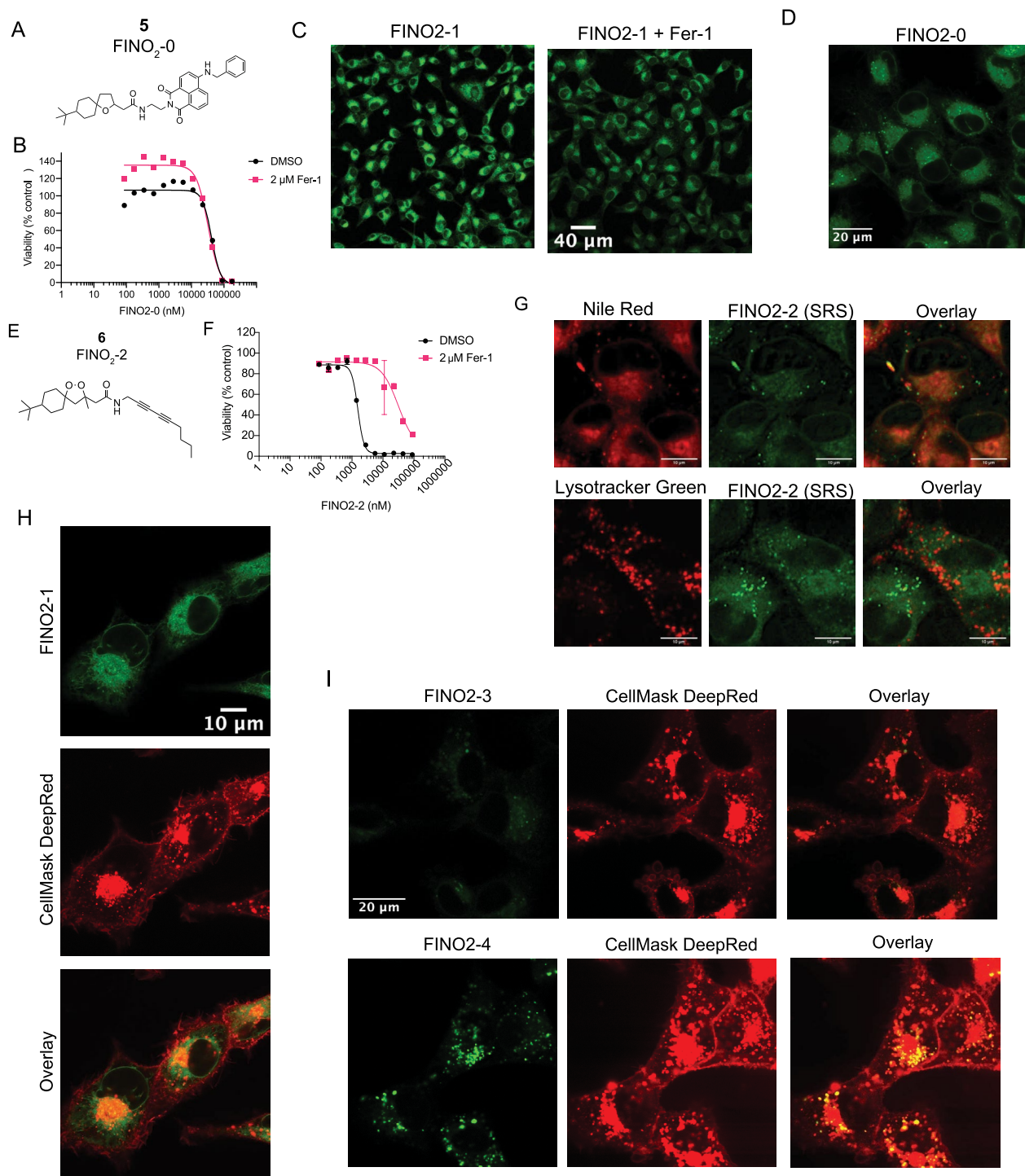
Extended Data Fig. 6 | FINO₂-0 and FINO₂-2 accumulate in the ER, and FINO₂-1/ FINO₂-3/FINO₂-4 do not accumulate in the plasma membrane. a. Structure of FINO₂-0. **b.** Dose-response curve of HT-1080 cells treated with FINO₂-0 ± fer-1. Data are represented as mean ± SEM, n=3. **c.** Confocal fluorescence images of HT-1080 cells treated for 3 hours with 3 μM FINO₂-1 alone or with 3 μM fer-1. **d.** Confocal fluorescence image of HT-1080 cells treated with 3 μM FINO₂-0. **f.** Confocal fluorescence imaging of HT-1080 cells treated with FINO₂-1 (3 μM) and fer-1 (3 μM) for 3 hours, co-stained with BODIPY TR ceramide. **g.** Structure of FINO₂-2. **h.** Dose-response curve of HT-1080 cells treated with FINO₂-2 ± fer-1. Data are represented as mean ± SEM, n=3. **i.** SRS and fluorescence imaging of HT-1080 cells treated with 20 μM FINO₂-2 and 2 μM fer-1, and stained with Nile Red and Lysotracker green. **j.** Confocal fluorescence image of HT-1080 cells treated with 3 μM FINO₂-1 and 3 μM fer-1, and costained with CellMask Deep Red. **k.** Confocal fluorescence image of HT-1080 cells treated with 3 μM FINO₂-3 or 3 μM FINO₂-4, and 3 μM fer-1, and co-stained with CellMask Deep Red.
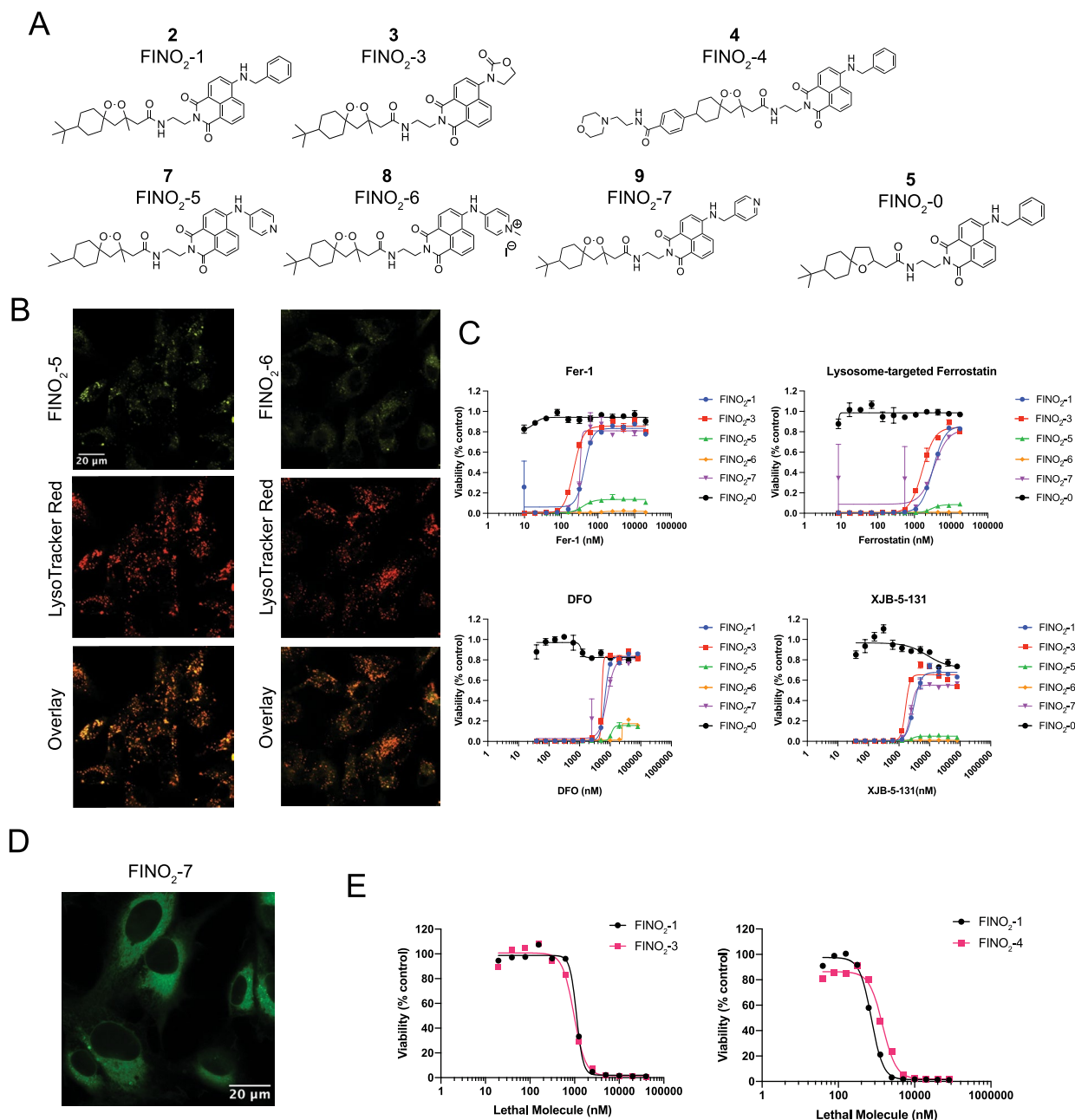
Extended Data Fig. 7 | Analogs of FINO$_2$ redistribute throughout the cell.
a. Structures of analogs of FINO$_2$. b. Confocal fluorescence images of HT-1080 cells treated with FINO$_2$-5 (3 μM) or FINO$_2$-6 (3 μM) and fer-1 (3 μM), and co-stained with LysoTracker Red. c. Dose-response curves of HT-1080 cells treated with fixed concentrations of FINO$_2$ analogs (10 μM) and varying concentrations of ferroptosis inhibitors. Lysosome-directed ferrostatin previously published by Gaschler et al.[27]. Data are represented as mean ± SEM, n=3. d. Confocal fluorescence image of HT-1080 cells treated with FINO$_2$-7 (3 μM) and fer-1 (3 μM). e. Dose-response curves of HT-1080 cells comparing treatment with FINO$_2$-1 and FINO$_2$-3 or FINO$_2$-4. Data are represented as mean ± SEM, n=3.
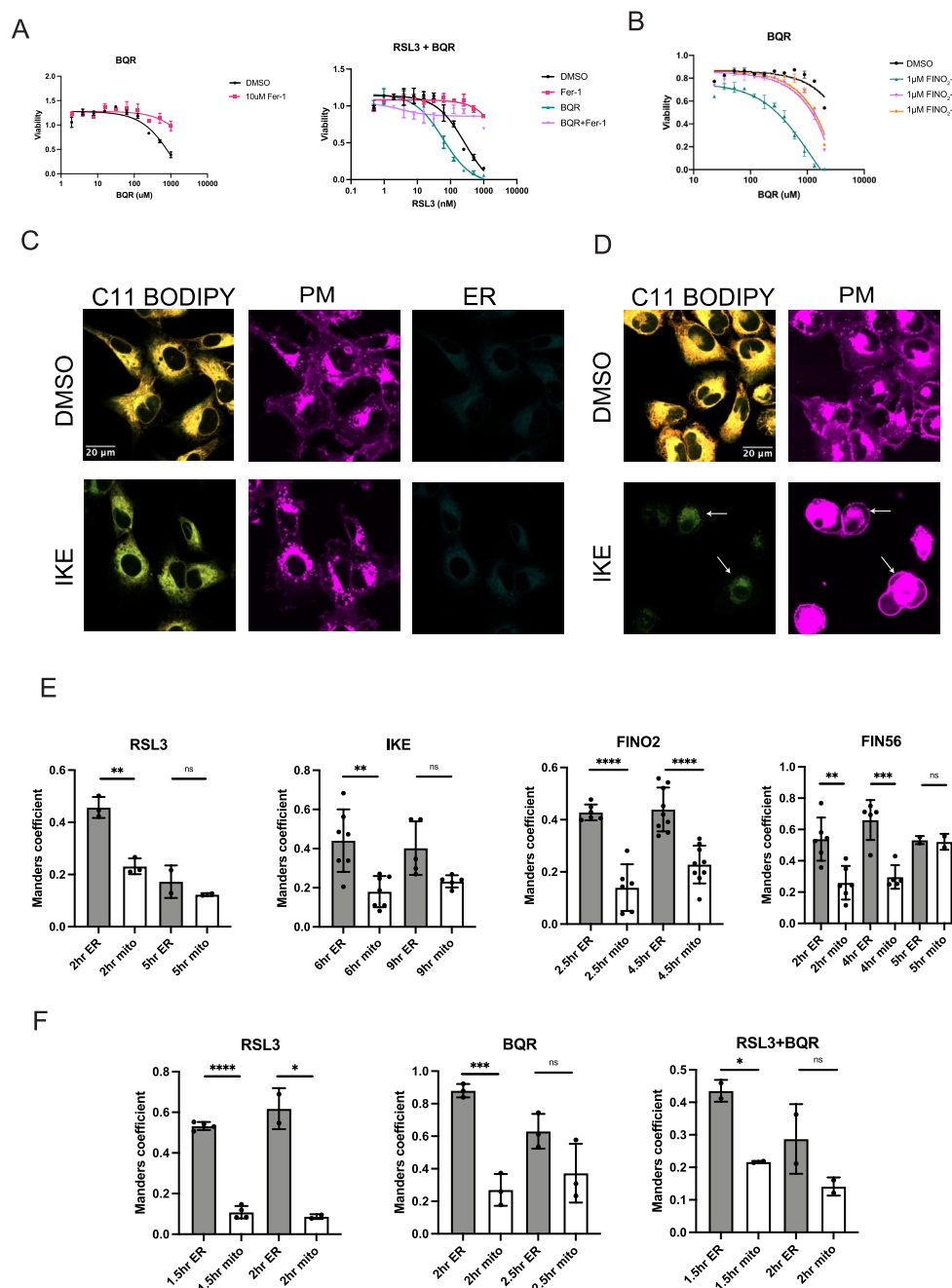
Extended Data Fig. 8 | Ferroptosis induced by DHODH inhibition is amplified by ER peroxidation, ferroptosis induced by IKE results in ER membrane peroxidation followed by PM peroxidation, early perinuclear lipid peroxidation occurs in the ER. a. Brequinar (BQR) induces ferroptosis in HT-1080 cells as rescued by fer-1, and cotreatment with BQR (500 μM) increases sensitivity to RSL3 in HT-1080 cells. Data are represented as mean ± SEM, n=3. **b.** Dose-response curve of HT-1080 cells cotreated with 1 μM of FINO$_2$-1, FINO$_2$-3, or FINO$_2$-4. Data are represented as mean ± SEM, n=3. **c.** HT-1080 cells treated with DMSO or IKE (10 μM) for 6 hours and stained with C11 BODIPY (oxidized and reduced overlay), CellMask Deep Red, and ERTracker Blue-White. **d.** HT-1080 cells treated with DMSO or IKE (10 μM) for 10 hours and stained with C11 BODIPY (oxidized and reduced overlay), CellMask Deep Red, and ERTracker Blue-White. **e.** Correlation (Manders coefficient) of C11 BODIPY oxidized signal with ERTracker Blue-White or MitoTracker Deep Red in HT-1080 cells treated with either RSL3, IKE, FINO$_2$, or FIN56 at designated timepoints. Data are represented as mean

± SEM, each individual point represents an image of multiple cells. Number of images for each condition are RSL3 2 hour (n=3), 5 hour (n=2); IKE 2 hour (n=7), 5 hour (n=5), FINO2 2.5 hour (n=6), 4.5 hour (n=9), FIN56 2 hour (n=6), 4 hour (n=5), 5 hour (n=2). Ordinary one way ANOVA with Tukey's test for multiple comparisons was used with p values of: RSL3 (0.0016, 0.6120), IKE (0.0023, 0.1279), FINO2 (<0.0001, <0.0001), FIN56 (0.0034, 0.0005, >0.9999). **f.** Correlation (Manders coefficient) of C11 BODIPY oxidized signal with ERTracker Blue-White or MitoTracker Deep Red in HT-1080 cells treated with either RSL3 (1 μM), BQR (1 mM) or both at designated timepoints. Data are represented as mean ± SEM, each individual point represents an image of multiple cells. Number of images for each condition are RSL3 1.5 hour (n=4), 2 hour (n=2); BQR 2 hour (n=3), 2.5 hour (n=3); RSL3 + BQR 1.5 hour (n=2), 2 hour (n=2). Two-sided unpaired t test was used with p values of: RSL3 (<0.0001, 0.0178), BQR (0.0006, 0.1011), RSL3 + BQR (0.0117, 0.2027). For all panels, GraphPad Prism (GP) P value style of 0.1234 (ns), 0.0332 (*), 0.0021 (**), 0.0002 (***), <0.0001 (****).

Corresponding author(s): Wei Min, K. A. Woerpel, Brent R. Stockwell

Last updated by author(s): August 25, 2022

Reporting Summary

Nature Portfolio wishes to improve the reproducibility of the work that we publish. This form provides structure for consistency and transparency in reporting. For further information on Nature Portfolio policies, see our Editorial Policies and the Editorial Policy Checklist.

Statistics

For all statistical analyses, confirm that the following items are present in the figure legend, table legend, main text, or Methods section.

n/a	Confirmed	
☐	☒	The exact sample size (n) for each experimental group/condition, given as a discrete number and unit of measurement
☒	☐	A statement on whether measurements were taken from distinct samples or whether the same sample was measured repeatedly
☐	☒	The statistical test(s) used AND whether they are one- or two-sided *Only common tests should be described solely by name; describe more complex techniques in the Methods section.*
☒	☐	A description of all covariates tested
☒	☐	A description of any assumptions or corrections, such as tests of normality and adjustment for multiple comparisons
☐	☒	A full description of the statistical parameters including central tendency (e.g. means) or other basic estimates (e.g. regression coefficient) AND variation (e.g. standard deviation) or associated estimates of uncertainty (e.g. confidence intervals)
☐	☒	For null hypothesis testing, the test statistic (e.g. F, t, r) with confidence intervals, effect sizes, degrees of freedom and P value noted *Give P values as exact values whenever suitable.*
☒	☐	For Bayesian analysis, information on the choice of priors and Markov chain Monte Carlo settings
☒	☐	For hierarchical and complex designs, identification of the appropriate level for tests and full reporting of outcomes
☒	☐	Estimates of effect sizes (e.g. Cohen's d, Pearson's r), indicating how they were calculated

Our web collection on statistics for biologists contains articles on many of the points above.

Software and code

Policy information about availability of computer code

Data collection	Zeiss Zen Blue 2.1
Data analysis	GraphPad Prism 9.2.0, FIJI 2.0.0, CellProfiler 3.1.9, MATLAB R2020a, MassLynx 4.1, R 3.4.4, XCMS 3.2.0, MSE Data Viewer 1.3

For manuscripts utilizing custom algorithms or software that are central to the research but not yet described in published literature, software must be made available to editors and reviewers. We strongly encourage code deposition in a community repository (e.g. GitHub). See the Nature Portfolio guidelines for submitting code & software for further information.

Data

Policy information about availability of data

All manuscripts must include a data availability statement. This statement should provide the following information, where applicable:
- Accession codes, unique identifiers, or web links for publicly available datasets
- A description of any restrictions on data availability
- For clinical datasets or third party data, please ensure that the statement adheres to our policy

The mass spectrometry raw data files are deposited to the Columbia Academic Commons and can be accessed at https://doi.org/10.7916/rphv-v394. Metlin can be accessed at https://massconsortium.com. LIPID MAPS can be accessed at https://www.lipidmaps.org. HMDB can be accessed at https://hmdb.ca. All other data is included as Source Data and can be accessed at https://doi.org/10.7916/hggm-7r90.

Field-specific reporting

Please select the one below that is the best fit for your research. If you are not sure, read the appropriate sections before making your selection.

$\boxtimes$ Life sciences $\square$ Behavioural & social sciences $\square$ Ecological, evolutionary & environmental sciences

For a reference copy of the document with all sections, see nature.com/documents/nr-reporting-summary-flat.pdf

Life sciences study design

All studies must disclose on these points even when the disclosure is negative.

Sample size	No sample size calculation was performed. For all viability experiments, a minimum sample size of 3 independent biological samples was used as is convention within the field and sufficient for calculating statistical significance. For imaging experiments, enough images were taken for sufficient cells to effectively evaluate statistical significance or lack thereof, resulting in at least 14 cells per condition for per cell experiments, or at least two images for Manders coefficient overlap. These sample sizes resulted in statistical significance with p values of <0.0001 indicating that sample size is likely sufficient. For all other studies, sample size of at least 3 was used, again as is convention in the field and resulting in statistically significant results.
Data exclusions	No data was excluded.
Replication	All attempts at replication reproduced the results. For all experiments a minimum of two independent replications was performed.
Randomization	Randomization was used in lipidomics for the order of running samples. For all other experiments, randomization was not required as there is no preferential allocation of certain cells in vitro, and thus the cells are inherently randomized.
Blinding	No in vivo studies were performed. Blinding does not typically occur in this type of in vitro experimentation, and many of the experiments were performed and analyzed by a single person making blinding not possible. Additionally, the quantitative output of the experiments is not affected by blinding as an observational study or survey would be.

Reporting for specific materials, systems and methods

We require information from authors about some types of materials, experimental systems and methods used in many studies. Here, indicate whether each material, system or method listed is relevant to your study. If you are not sure if a list item applies to your research, read the appropriate section before selecting a response.

Materials & experimental systems

n/a	Involved in the study
$\square$	$\boxtimes$ Antibodies
$\square$	$\boxtimes$ Eukaryotic cell lines
$\boxtimes$	$\square$ Palaeontology and archaeology
$\boxtimes$	$\square$ Animals and other organisms
$\boxtimes$	$\square$ Human research participants
$\boxtimes$	$\square$ Clinical data
$\boxtimes$	$\square$ Dual use research of concern

Methods

n/a	Involved in the study
$\boxtimes$	$\square$ ChIP-seq
$\boxtimes$	$\square$ Flow cytometry
$\boxtimes$	$\square$ MRI-based neuroimaging

Antibodies

Antibodies used	Mouse monoclonal anti-ACSL4 (F-4) from Santa Cruz Biotechnology Cat# sc-365230. Rabbit monoclonal anti-Pan-Actin (D18C11) from Cell Signaling Technology, Cat# 8456. Mouse monoclonal anti-β-Actin (8H10D10) (Cell Signaling Technology), Cat #3700. Rabbit monoclonal anti-Cytochrome c (D18C7) (Cell Signaling Technology), Cat #11940. Rabbit Monoclonal anit-PDI (C81H6) (Cell Signaling Technology) #3501, IRDye Goat Anti-Mouse 680, IRDye Goat Anti-Rabbit 800 antibodies (LICOR), mouse anti-ACSL4 antibody (Invitrogen PA5-27137), rabbit anti-Calnexin antibody (Invitrogen MA3-027), Alexafluor 594-conjugated anti-mouse (Invitrogen A-11032) and Alexafluor 488-conjugated anti-rabbit antibody (Invitrogen A11006).
Validation	All commercial antibodies were rigorously validated by their distributors for functionality, sensitivity, and specificity. They are all demonstrated to be effective across multiple cell lines and cited in numerous publications. For Cell Signaling Technology, western blotting was validated by testing in multiple cell lines, using growth factors/chemical activators/inhibitors to modulate expression and confirm specificity, using siRNA or KO cell lines to verify specificity, side-by-side comparison for lot-lot consistency, and optimal dilution predetermination. Santa Cruz antibodies are validated by testing in multiple cell lines, including over-expression cell lines showing an increase in specific signal. LICOR antibodies are isolated by affinity chromatography and then confirmed for specifity by ELISE and flow cytometry, as well as tested for cross-reactivity by dot blot and/or solid phase adsorption, then specifically tested and qualified in Western blotting. Invitrogen antibodies are tested for specificity using at minimum one method including knockout, knockdown, cell treatment, relative expression, neutralization, peptide array, SNAP-ChIP, or Immunoprecipitation Mass Spectrometry, and then confirmed for effectiveness for their application of interest (in this case immunofluorescence imaging).

Eukaryotic cell lines

Policy information about [cell lines](#)

Cell line source(s)	All cell lines were obtained from ATCC. These cell lines include HT1080, PANC-1, HEK293T, N27, and HT22.
Authentication	The cell lines were not authenticated.
Mycoplasma contamination	All cells are negative for mycoplasma.
Commonly misidentified lines (See [ICLAC](#) register)	No commonly misidentified lines were used.